



The Role of Deposition of Cosmogenic ^{10}Be for the Detectability of Solar Proton Events

K. Schaar¹, T. Spiegl^{1,2} , U. Langematz¹ , T. Sato³ , F. Mekhaldi^{4,5} , M. Kunze⁶,
F. Miyake⁷ , and S. Yoden^{8,9} 

¹Institut für Meteorologie, Freie Universität Berlin, Berlin, Germany, ²Alfred-Wegener-Institut, Bremerhaven, Germany, ³Japan Atomic Energy Agency, Tokai, Japan, ⁴Department of Geology – Quaternary Sciences, Lund University, Lund, Sweden, ⁵Aix-Marseille Université, CNRS, IRD, INRAE, CEREGE, Aix-en-Provence, France, ⁶Leibniz-Institut für Atmosphärenphysik, Kühlungsborn, Germany, ⁷Institute for Space-Earth Environmental Research, Nagoya University, Nagoya, Japan, ⁸Graduate School of Science, Kyoto University, Kyoto, Japan, ⁹Institute for Liberal Arts and Sciences, Kyoto University, Kyoto, Japan

Key Points:

- The role of galactic cosmic rays for the detectability of solar proton events in Beryllium-10 ice core records was studied in a 3D-model
- We show that sedimentation can be a major deposition mechanism for Beryllium-10, especially at high latitudes
- The seasonal timing of the solar proton event and the phase of the 11-year solar cycle during the event have an impact on its detectability

Correspondence to:

U. Langematz,
ulrike.langematz@fu-berlin.de

Citation:

Schaar, K., Spiegl, T., Langematz, U., Sato, T., Mekhaldi, F., Kunze, M., et al. (2024). The role of deposition of cosmogenic ^{10}Be for the detectability of solar proton events. *Journal of Geophysical Research: Atmospheres*, 129, e2023JD040463. <https://doi.org/10.1029/2023JD040463>

Received 22 NOV 2023
Accepted 18 MAY 2024

Abstract The manifestation of extreme solar proton events (SPEs) in Beryllium-10 (^{10}Be) ice core data contains valuable information about the strength and incidence of SPEs or local characteristics of the atmosphere. To extract this information, the signals of enhanced production of cosmogenic ^{10}Be due to the SPEs have to be detected, hence distinguished from the variability of the background production by galactic cosmic rays (GCRs). Here, we study the transport and deposition of ^{10}Be from GCRs, using the ECHAM/MESSy Atmospheric Chemistry climate model, and discuss the detectability of extreme SPEs (similar to the CE 774/775 SPE) in ^{10}Be ice core data depending on the ice core location, seasonal appearance of the SPE, atmospheric aerosol size distribution and phase of the 11-year solar cycle. We find that sedimentation can be a major deposition mechanism of GCR generated ^{10}Be , especially at high latitudes, depending on the aerosols to which ^{10}Be attaches after production. The comparison of our results to four ice core records of ^{10}Be from Greenland and Antarctica shows good agreement for both ^{10}Be from GCRs and solar energetic particles (SEP). From our results we deduce that the location of detection and the season of occurrence of the SPE have a considerable effect on its detectability, as well as the aerosol size distribution the produced cosmogenic nuclides meet in the atmosphere. Furthermore, we find that SPEs occurring in the phase of highest activity during the 11-year solar cycle are more detectable than SPEs that arise in the phase of lowest activity.

Plain Language Summary Solar proton events are eruptions of particles from the Sun that can cause an increased production of Beryllium-10 in Earth's atmosphere. This increase can be detected in ice cores, which can tell us about the dynamics of the Sun or local characteristics of the atmosphere. To detect solar proton events in ice cores, the signal must be distinguished from the background production of Beryllium-10 from galactic cosmic rays, because the two signals can be very similar. Here, we used a climate model to study the deposition of Beryllium-10 from galactic cosmic rays and simulated the detectability of solar proton events in ice cores for different locations, months of occurrence, sizes of aerosols in the atmosphere, and phases of the 11-year solar cycle. We found that sedimentation can be a major deposition mechanism for Beryllium-10, especially at high latitudes. We also found that the season of the solar proton event has a big impact on its detectability. Furthermore, we show that solar proton events that occur during high solar activity are more easily detected than events that occur during a phase of low activity. The findings are useful to improve the interpretation of Beryllium-10 ice core records.

1. Introduction

Various cosmogenic nuclides, for example, Beryllium-10 (hereafter ^{10}Be), Beryllium-7 or Carbon-14 (hereafter ^{14}C), are constantly produced by nuclear reactions of energetic particles, that is, galactic cosmic rays (GCRs) and solar energetic particles (SEPs) (e.g., Masarik & Beer, 1999), with molecules of the atmosphere. While GCRs produce cosmogenic nuclides continuously, extreme SEP events contribute to the production of massive amounts of cosmogenic nuclides in the atmosphere sporadically. This could lead to significant peaks of the ^{10}Be concentration in natural archives, such as ice cores from Antarctica and Greenland (e.g., Mekhaldi et al., 2015; Sigl et al., 2015) or of the ^{14}C concentration in tree rings (e.g., Miyake et al., 2012, 2013). Due to the long half-life of ^{10}Be (1.387 million years), it conserves the imprints of the cosmogenic isotope on quaternary timescales in the

© 2024 The Authors.

This is an open access article under the terms of the [Creative Commons Attribution-NonCommercial License](https://creativecommons.org/licenses/by-nc/4.0/), which permits use, distribution and reproduction in any medium, provided the original work is properly cited and is not used for commercial purposes.

polar regions where ice cores can be extracted. The concentration of ^{14}C in tree rings, in contrast, can be extracted over a broad range of latitudes, but has a lower temporal extension due to the shorter half-life of ^{14}C (approx. 5,730 years).

One of the most intense SPEs of the last two thousand years is the CE 774/775 SPE (Miyake et al., 2012), which has been subject to multiple studies (e.g., Mekhaldi et al., 2015; Melott & Thomas, 2012; Spiegl et al., 2022; Usoskin et al., 2013). Other SPE candidates have been detected as well in natural archives, for example, for BCE 7176 (Brehm et al., 2022; Paleari et al., 2022), BCE 5410 (Miyake et al., 2021), BCE 5259 (Brehm et al., 2022), BCE 660 (O'Hare et al., 2019; Park et al., 2017; Sakurai et al., 2020), CE 1279 (Brehm et al., 2021; Miyahara et al., 2022), CE 1052 (Brehm et al., 2021; Terrasi et al., 2020), and CE 993 (Büntgen et al., 2018; Mekhaldi et al., 2015; Miyake et al., 2013). Common to all these studies is that the signal of the SPE in natural archives had to be distinguished from the background variability of the cosmogenic nuclides from GCR. One important factor in this regard is the amount (intensity) and energy spectrum (hardness) of the protons of the SPE, which determines the production rate of cosmogenic nuclides (Mekhaldi et al., 2021; Usoskin et al., 2020). Mekhaldi et al. (2021) state that it is unlikely to detect any recent SPE in ^{10}Be from ice cores because these SPEs were not intense and hard enough to leave an attributable imprint from GCR background. Therefore, ^{10}Be may be only suitable to detect a limited number of extreme SPEs (with a hard spectrum). This implies that estimates of the occurrence rate of extreme solar storms, based mainly on ^{10}Be (and ^{14}C , like in the aforementioned papers), capture only a small number of potential SPEs and the probability of extreme solar storms to hit Earth may be greater than ^{10}Be and ^{14}C data imply. Note that for example, Chlorine-36 (hereafter ^{36}Cl), might be more suitable to detect SPEs with a softer energy spectrum, because the relative increase of the production rate of the isotope due to such SPEs compared to the GCR background is larger than for ^{10}Be (Mekhaldi et al., 2021). Contrary to ^{10}Be , ^{36}Cl production has a production channel from low-energy particles. More details about extreme solar events are provided in the recent review by Usoskin et al. (2023).

To detect SPEs, the amount of cosmogenic nuclides produced by the SPE has to exceed the variability of nuclide production by GCR due to solar modulation (e.g., the 11-year solar cycle). The quantity of GCR production and the energy spectrum of GCR penetrating the atmosphere of the Earth are mainly driven by heliospheric shielding and the geomagnetic activity (Usoskin, 2017). Hence, the amount of cosmogenic nuclides produced in the atmosphere by GCR and thus the concentration of cosmogenic isotopes in natural archives can vary in time according to different activity cycles of the Sun, especially the 11-year solar cycle. In phases of higher solar activity, with a large number of sunspots and a high modulation potential ϕ (which is a parametric representation of the impact of the heliosphere on GCR (Gleeson & Axford, 1968)), the production of cosmogenic isotopes is lower, because GCR is shielded more by the stronger magnetic field of the Sun. In phases of lower solar activity, with a lower number of sunspots and low modulation potential ϕ , the production of cosmogenic isotopes is higher due to less magnetic shielding (Usoskin, 2017). The intensity of GCR and thus the production of cosmogenic isotopes also varies on longer time scales due to solar activity changes over decades and centuries (Usoskin et al., 2006). Thus, because of these mechanisms the variation of the concentration of cosmogenic isotopes in natural archives can be used as a proxy for the variability of the solar activity (Beer et al., 1994).

The variability of the concentration of cosmogenic isotopes in natural archives arises not only from solar activity but also from (a) the transport of the isotopes in the atmosphere and (b) their deposition at Earth's surface (e.g., Spiegl et al., 2022). In the following this will be explained only for ^{10}Be , because other cosmogenic isotopes are not subject of this paper. Typically, over 60% of cosmogenic ^{10}Be from GCR is produced above the tropopause (Golubenko et al., 2022), with the majority of ^{10}Be being produced in the lower stratosphere at higher latitudes due to the structure of the geomagnetic field and the energy spectrum of GCR (Heikkilä et al., 2013). Shortly after production, ^{10}Be attaches mainly to stratospheric aerosols, mostly sulfuric acid droplets from the Junge layer, which is a layer formed by photochemical oxidation of sulfur dioxide from volcanic sources at 15–20 km (Junge, 1963). The mean radius of stratospheric aerosols is in the range from 0.05 to 0.1 μm but can also change considerably during profound volcanic eruptions (Malinina et al., 2018). The stratospheric mean meridional circulation, the Brewer-Dobson Circulation (BDC), then transports and mixes the cosmogenic ^{10}Be from lower latitudes toward the poles (Butchart, 2014). The BDC describes the net transport of air mass in the middle atmosphere (which lies between the mesopause at about 90 km altitude and the tropopause) and incorporates two components, (a) the horizontal mixing of air and (b) a mean meridional circulation (MMC), described by the Transformed Eulerian mean (TEM) meridional and vertical residual velocities (e.g., Andrews et al., 1987; Oberländer-Hayn et al., 2015). Both components are driven by wave disturbances propagating upward from the

troposphere in the respective winter and spring seasons. These perturbations propagate as waves (mostly large-scale planetary) with an increasing amplitude over height until they break in the stratosphere, thereby inducing a MMC with upward transport in the tropics as well as in the summer hemisphere and a poleward-downward transport in the winter stratosphere. Differences in the planetary wave generation in the Northern Hemisphere (NH) and Southern Hemisphere (SH) troposphere finally lead to a stronger transport by the MMC in northern winter and spring relative to the corresponding southern season (Delaygue et al., 2015; Spiegl et al., 2022).

The tropopause acts as a barrier for vertical transport toward the troposphere, thus forming a stratospheric reservoir of ^{10}Be above the tropopause (see e.g., Beer et al., 2012). As a result, the cosmogenic ^{10}Be resides in the stratosphere for a period of around 1–2 years on average (Feely et al., 1966) until it is injected to the troposphere by stratosphere-troposphere exchange (STE) processes. STE is associated with tropopause folds and cut-off lows, for example, in the vicinity of the tropospheric jets, and impacted by the strength of the BDC and tropospheric synoptic and mesoscale variability in the extratropics (Appenzeller et al., 1996; Holton et al., 1995; Stohl et al., 2003). After its transport into the troposphere, ^{10}Be is transported to the surface relatively fast by vertical convective transport, for example, at the Hadley-Ferrel convergence zone (HFCZ), by synoptic dynamics and small-scale convective mixing. The residence time of aerosols in the upper troposphere ranges from 20 to 40 days, while close to the surface it is only a few days (Yamagata et al., 2019). The mean residence time in the troposphere as a whole thus ranges from a few weeks to a few days, depending also on the size of the tropospheric aerosols, which covers a large range from several nanometers to 100 μm and more (Pandis et al., 1995).

The deposition of cosmogenic ^{10}Be at the surface is determined by three mechanisms: wet deposition, dry deposition and sedimentation. Wet deposition occurs in the lower troposphere, in regions of high precipitation and cloud formation by impact scavenging and nucleation scavenging. Impact scavenging is defined as the atmospheric washout of aerosols by precipitation from above (below-cloud scavenging) and is the most dominant form of wet deposition in the tropics, where (convective) precipitation is high throughout the year. Nucleation scavenging of aerosols describes the dissolution of aerosol particles into water droplets inside clouds (in-cloud scavenging), during the nucleation and growth of cloud droplets by microphysical processes that can result in precipitation formation (Ohata et al., 2016; Tost et al., 2006). Nucleation scavenging of cosmogenic ^{10}Be is present, when the concentration of such aerosols carrying the isotope is large in layers of the atmosphere where the formation of clouds happens. This is for example, the case for the storm track region, a global band in the higher latitudes on both hemispheres, where synoptic activity is relatively high and a lot of (large-scale) precipitation occurs. Dry deposition describes a process at the surface, where the intensity of the deposition is a result of surface friction, influenced by for example, vegetation cover and surface roughness, and local surface winds both controlling near surface turbulence (Kerkweg et al., 2006). In regions with low precipitation rates, like the coastal deserts in South Africa and South America, or the polar latitudes, dry deposition can exceed wet deposition and plays a major role for the deposition of cosmogenic ^{10}Be (Field et al., 2006; Heikkilä et al., 2013). Sedimentation, which is defined as the downward motion of particles due to gravitation, affects aerosols throughout the entire vertical column of the atmosphere and can be an important deposition mechanism for ^{10}Be attached to larger aerosols.

All these effects of atmospheric transport and deposition are imprinted in the cosmogenic ^{10}Be stored in ice cores, as for example, shown by Zheng et al. (2020). To further extract this information and reveal more details about the role of the mechanism involved, extended studies including computer simulations of the transport and deposition of ^{10}Be are required. In contrast to experimental studies with natural archives, which are often limited to yearly resolution of the data and only few additional information about the context of the data, numerical studies allow to control all conditions of the production, transport and deposition of ^{10}Be from GCR and SPE, such as for example, the production rates of GCR and the phase of the 11-year solar cycle, the season of the occurrence of the SPE and the distribution of aerosols in the atmosphere. The use of a numerical model allows us to entangle the several factors combined in the signals in natural archives, produce high resolution data and compare the results to measurements.

Former studies on this subject (e.g., Field et al. (2006) with the NASA GISS Model E General Circulation Model (GCM), or simulations by Heikkilä et al. (2008) using the ECHAM5-HAM climate model) have provided important contributions to the current knowledge of the global atmospheric distribution and deposition patterns of ^{10}Be from GCR under changing solar, geomagnetic and atmospheric conditions, such as the Maunder Minimum (Heikkilä et al., 2008), higher CO_2 concentrations in the atmosphere or a geomagnetic minimum (Field

et al., 2006). Both studies agree that, although the concentration of ^{10}Be in ice cores is strongly affected by production, the inference of changes in the production signal from natural archives is complex, since it is influenced by multiple factors (e.g., STE, tropospheric transport and mixing, and precipitation). However, all of these approaches have limitations, for example, the degree of global mixing of ^{10}Be in the atmosphere, or a coarse vertical model resolution of 20 layers with a model top in the lower mesosphere (0.1 hPa), or an underestimation of the lower stratospheric variability and STE. Furthermore, they do not include signals from SPEs or address their detectability under different conditions. Sukhodolov et al. (2017) simulate the surface flux of ^{10}Be from the CE 774/775 SPE in ice cores, but miss wet deposition as well as sedimentation due to a simplified gaseous tracer description. The study by Mekhaldi et al. (2021) using box outputs from a GCM gives valuable insight on the general detectability of SPEs according to their energy spectrum and intensity, but does not include differentiated locations, nor addresses the impact of seasonality, different aerosol settings or the phase of the 11-year solar cycle. In addition, the deposition model used in their study is very basic and does not include individual deposition mechanisms like wet and dry deposition or sedimentation.

Here, we go further and extend our work from Spiegl et al. (2022) to investigate the transport and deposition of ^{10}Be produced by GCR as the basis to study the detectability of SPEs, such as the extreme CE 774/775 SPE, under different solar and atmospheric conditions. By analyzing targeted simulations of a 3-dimensional chemistry-climate model (CCM), we will address the following topics:

1. The dependence of the deposition of ^{10}Be on the distribution of the size of the stratospheric and tropospheric aerosols, including the zonal-mean and global deposition pattern of ^{10}Be from GCR for different deposition mechanisms in individual seasons.
2. The correlation between the vertical tracer distribution of ^{10}Be , precipitation and wet deposition as well as the correlation between near surface wind speed and dry deposition and the relevance of sedimentation.
3. The comparison of our model results for the CE 774/775 SPE with GCR background production to ^{10}Be data from ice cores at different drilling sites from Greenland and Antarctica.
4. The detectability of the CE 774/775 SPE compared to the GCR background variability for different locations, phases of the solar cycle, seasons and aerosol settings.

In Section 2 we describe the modeling approach used as well as the methods (a) to extend our former simulations from Spiegl et al. (2022) with time-varying ^{10}Be production from GCR and (b) to describe ^{10}Be as a passive tracer attached to aerosols with different aerosol radius distribution for the stratosphere and troposphere. In Section 3 we discuss the modeled zonal-mean and global deposition patterns of ^{10}Be from GCR. Section 4 contains a comparison of our model simulations for the CE 774/775 SPE including a GCR background to ^{10}Be ice core data from Greenland and Antarctica. Additionally, we discuss in this section the detectability of the CE 774/775 SPE depending on different GCR background conditions, the seasonal timing of the SPE occurrence, the size distribution of aerosols and the respective phase of the 11-year solar cycle during the SPE. Section 5 includes a summary and discussion.

2. Model Setup and Methods

As in Spiegl et al. (2022), our passive tracer experiments were carried out with the chemistry-climate model ECHAM/MESSy Atmospheric Chemistry (EMAC) (Jöckel et al., 2016), which is based on the European Centre Hamburg general circulation model 5 (ECHAM5) (Roeckner et al., 2006) and the modular Earth submodel system (MESSy) model version 2.55. The MESSy interface (Jöckel et al., 2010) is a modular submodel system that allows the simulation of various chemical and physical processes that are important for the transport and deposition of cosmogenic nuclides. The simulations were conducted using a horizontal/vertical resolution of T42L47MA, corresponding to a Gaussian grid of 2.8 by 2.8° in latitude and longitude (triangular spherical harmonics truncation of T42) and 47 layers in height (L47), with the model upper boundary at 0.01 hPa (~80 km, middle atmosphere). The physical parameterizations of for example, radiative transfer, are described in Spiegl et al. (2022) and references therein. To describe the processes specific to our simulations on cosmogenic ^{10}Be , we incorporate several MESSy modules, explained in the following sections. Each simulation starts with a spin-up phase of 2 years to overcome the initial imprint of the initialization fields and stabilize the atmospheric dynamics.

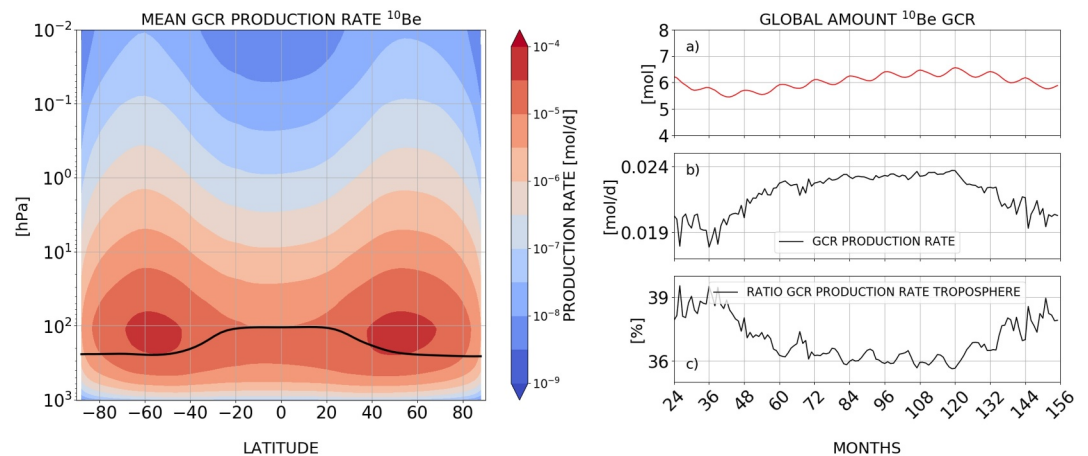


Figure 1. Left: Zonal-mean GCR-production rate of ¹⁰Be [mol/d] averaged over one 11-year solar cycle (2009–2020) as a function of latitude and pressure based on the PARMA/PHITS model. Right: (a) Global monthly mean of ¹⁰Be [mol] produced by GCR after a spin-up phase of 2 years (24 months) for one cycle of the 11-year solar cycle (132 months). The global amount shows a decadal oscillation due to the 11-year solar cycle as well as annual oscillations resulting from seasonal variability of deposition. (b) Global GCR production rate [mol/d] over time, with the 11-year solar cycle (2009–2020) phase shifted such, that the production rate is in near the minimum after the spin-up phase. (c) Fraction of cosmogenic ¹⁰Be being produced in the troposphere over time. Panels (a)–(c) show the GCRmin scenario. For the GCRmax scenario the plots look identical but are shifted such, that they start with the production rate maximum.

2.1. Implementation of GCR

Cosmogenic ¹⁰Be is continuously produced by GCR due to spallation of, for example, Nitrogen-14 and Oxygen-16 (hereafter ¹⁴N and ¹⁶O) by energetic particles, with spatio-temporal varying production rates (Kovaltsov & Usoskin, 2010). The 3-dimensional GCR-production rates of ¹⁰Be used as input data for our simulations have been calculated using the Particle and Heavy Ion Transport code System (PHITS) based Analytical Radiation Model in the Atmosphere (PARMA) approach, coupled with their production cross sections from atmospheric constituents (¹⁴N and ¹⁶O) evaluated by PHITS (Sato, Iwamoto, et al., 2018). See also <https://phits.jaea.go.jp/expacs/> and <https://phits.jaea.go.jp/> for further information, Sato et al. (2008) and Sato (2015, 2016) for information on PARMA and Lifton et al. (2014) for information on the application of PARMA for cosmogenic nuclide production.

The data contains the daily production rate of ¹⁰Be for the first of each month for the time span 1950 to 2020 (e.g., 1/1/1950, 1/2/1950, 1/3/1950, etc.), which is representative for every day of this time span, because on average the daily variations of global GCR production are small compared to annual and decadal variations. The amount of GCR reaching the magnetosphere of the Earth is directly influenced by the solar modulation potential ϕ (see Section 1). The modulation potential for preindustrial time periods is not known exactly, but Usoskin (2017) suggest that for the CE 774/775 SPE, ϕ is approximately between 300 and 600 MV. The production rates associated with these historical values of ϕ are in good agreement with those covering the period 2009–2020, with values approximately between 400 and 600 MV (Usoskin, 2017). Therefore, we use the production rates of ¹⁰Be for this time span from the data as a representation of the CE 774/775 GCR background. However, we use two different GCR background scenarios. (a) The GCRmin scenario, in which the 11-year solar cycle (2009–2020) is shifted such, that the simulation is near the minimum of the production rate after a spin-up phase and (b) the GCRmax scenario, in which the 11-year solar cycle is shifted such, that the simulation is near the maximum of the production rate after a spin-up phase. The precalculated 3-dimensional production rates are then imported to the model using the OFFEMIS submodel (Kerkweg et al., 2006).

Figure 1 shows the GCR production rate features used in all following simulations. The left plot in Figure 1 shows the zonal-mean GCR-production rate for ¹⁰Be over pressure in our simulation. The amount of ¹⁰Be produced in the stratosphere adds up to 63% and the majority is located in the mid-latitudes directly above the tropopause (black line, World Meteorological Organization (WMO) definition). The panel (a) on the right side of Figure 1 shows the resulting global amount of ¹⁰Be from GCR production. The two lower panels (b) and (c) show the variation of GCR-production rate over the shown time interval for GCRmin and the percentage of ¹⁰Be that is

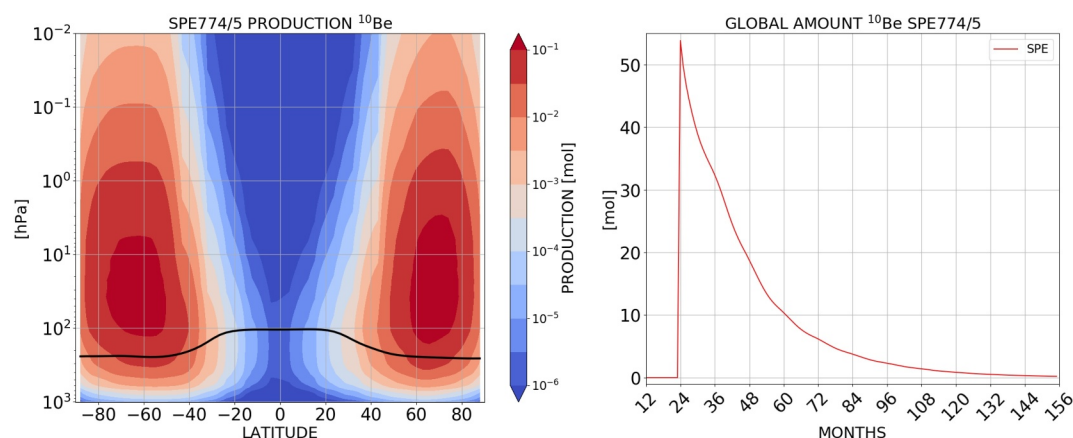


Figure 2. Left: Zonal-mean ¹⁰Be initial field [mol] produced by the CE 774/775 SPE. Right: Global amount of ¹⁰Be [mol] in the atmosphere produced by the SPE introduced in January from the occurrence of the SPE (first January after spin-up phase of 24 months) to the almost entire decay of the signal of the SPE.

produced in the troposphere. It can be seen, that for lower production rates, the amount of ¹⁰Be produced in the troposphere is higher, because the heliospheric shielding is stronger in these phases, thus the more energetic particles from the GCR-spectrum are more likely to reach the Earth than particles with lower energy, but then penetrate deeper into the atmosphere, producing more ¹⁰Be closer to the surface (Beer et al., 1994). Furthermore, the fluctuation of the production rate is higher in phases of lower production.

2.2. Implementation of SPE

Besides the continuous signatures of GCR, peaks of high isotope concentrations can be detected in natural archives as a result of particularly strong SPEs. However, the detection is only possible if the signal due to the SPEs significantly exceeds the variability of the GCR background production. In this context, the CE 774/775 SPE, is considered to be one of the strongest SPE during the Holocene and was first discovered by Miyake et al. (2012) by peaks of cosmogenic ¹⁴C concentrations in tree rings from Yakushima, Japan.

In this paper, we extend the simulations for the CE 774/775 event performed in our previous study (Spiegel et al., 2022) by introducing a fully simulated GCR background of ¹⁰Be and an improved simulation set-up incorporating nucleation scavenging, a variable aerosol background and a higher scaling factor of the SPE. This extended approach allows us to investigate also the detectability of different SPEs by relating the spatio-temporal deposition pattern of cosmogenic ¹⁰Be produced by the SPE introduced at different months to the background deposition pattern produced by GCR for different aerosol settings, as shown in Section 4.

As in Spiegel et al. (2022), the amount of cosmogenic ¹⁰Be produced by the CE 774/775 SPE is calculated based on spectrum data of the January 2005 ground level enhancement number 69 (GLE#69) using the PARMA approach (which is also implemented in the Warning System for Aviation Exposure to SEP [WASAVIES], see also Sato, Kataoka, et al., 2018). However, this time we use a linear scaling factor of 600 instead of 130, because recent studies from Mekhaldi et al. (2021) and Koldobskiy et al. (2023) suggest that the former medium range of scaling factors (119–141) for the GLE#69 compared to the CE 774/775 SPE estimated in Mekhaldi et al. (2015) might be considerably too small and the estimated fluence of the CE 774/775 SPE (>30 MeV) compared to the same fluence for GLE#69 gives a scaling factor of around 600, which also improves the accordance of our simulations with the ice core data.

As shown on the left side of Figure 2, the majority of ¹⁰Be from the SPE is produced above the tropopause (92%), which is similar to the values for the strong SPE GLE#5 given in Golubenko et al. (2022), and much more than for GCR. The reason for this is that the particle radiation of GCR is more energetic than the SEP from SPEs (Golubenko et al., 2022) and thus penetrates deeper into the atmosphere, producing much more ¹⁰Be below the tropopause (37% for GCR vs. 8% for SPEs).

The panel on the right side of Figure 2 shows the global amount of ¹⁰Be in the atmosphere for the CE 774/775 SPE introduced on the first of January after two years (24 months) of spin-up phase. The decrease of the global amount

Table 1
Mean Radius R and Standard Deviation σ of the Tropospheric Aerosol Size Distributions Used in the Simulations

Tracer	T1	T2	T3	T4
R [μm]	0.1	0.1	0.6	1.0
σ	1.4	2.0	2.0	2.0

of ^{10}Be produced by the SPE slightly varies with the month of the tracer introduction, because the atmospheric background conditions that control the downward transport and deposition vary, depending on the respective season the SPE meets (for more details see Section 2.4).

2.3. ^{10}Be Tracer Description

^{10}Be is described as a passive aerosol-like tracer in the model, because the ^{10}Be produced in the atmosphere attaches to aerosols shortly after the production and follows its trajectories from the higher atmosphere to the surface (e.g., Delaygue et al., 2015). To define the physical properties of our tracers, we use the submodel PTRAC (Jöckel et al., 2008), which also includes a simplified aerosol model based on a lognormal distribution representation of the aerosol particle size (Equation 1 in Malinina et al., 2018) with mean radius R and standard deviation σ . As shown in Section 2.1, a large amount of ^{10}Be isotopes from GCR is produced in the troposphere (about 37%) and thus attached to tropospheric aerosol. To account for differences in the size distributions of aerosols in the stratosphere and troposphere, we assume that the isotopes produced above the tropopause couple to a different aerosol distribution than the isotopes produced in the troposphere.

The isotopes produced in the stratosphere couple mainly to aerosols from the Junge layer (e.g., sulfuric acid and water droplets) with an unperturbed size distribution (no volcanic background aerosols) of approximately $R = 0.1 \mu\text{m}$ and $\sigma = 1.4$ (Deshler, 2008). This is the stratospheric aerosol size distribution (S1) used in our simulations. Note that this is a slight modification to Spiegl et al. (2022), where $R = 0.08 \mu\text{m}$ and $\sigma = 1.6$ from Malinina et al. (2018) was used.

The tropospheric aerosols are manifold (e.g., water droplets, sea salt, dust, pollen, volcanic aerosols) and thus range in size from submicron to $>100 \mu\text{m}$ (Pandis et al., 1995). Therefore, we tested different aerosol size distributions for the troposphere, ranging from a distribution equal to the stratospheric distribution to broader distributions including larger aerosols. The mean radius R and standard deviation σ of the tropospheric aerosol size distributions T1, T2, T3, and T4 considered in our simulations are given in Table 1.

With these distributions, different tracer setups can be combined by summing the isotopes produced in the stratosphere and troposphere to represent all tracers in the atmosphere, as shown in Table 2.

The purpose of the GCRmin/GCRmax tracer settings is to test the influence of the phase of the 11-year solar cycle (max vs. min) on the detectability of the SPE signal. The results are shown in Section 4.

For the aerosol density, we chose $1,500 \text{ kg/m}^3$ for all simulations, to match the typical range ($500\text{--}3,000 \text{ kg/m}^3$) (Kerkweg et al., 2006). For the ^{10}Be produced by the SPE the stratospheric aerosol size distribution S1 was prescribed for the entire atmosphere, since the majority is produced above the tropopause ($>90\%$, see Section 2.2).

Due to the description of the cosmogenic ^{10}Be as an aerosol tracer, the deposition processes (wet and dry deposition and sedimentation) for aerosols apply. Sedimentation due to gravitational settling of the aerosol particles throughout the whole atmosphere is considered using a zeroth order upwind scheme (implemented in the submodel SEDI (Kerkweg et al., 2006)) with a sedimentation velocity based on the Stokes velocity corrected for aspherical particles (Kerkweg et al., 2006). Wet deposition is described by the submodel SCAV (Tost et al., 2006) incorporating impact scavenging and nucleation scavenging (for more details see Tost et al., 2006). Dry deposition of ^{10}Be containing aerosol particles is applied at the lowest model level. The submodel DDEP calculates dry deposition velocities depending on the near-surface friction, wind speed and further physical and chemical

Table 2
Combinations of Stratospheric and Tropospheric Aerosol Size Distributions Used in the Model Simulations as Different Tracer Setups

Simulations	GCRminSMALL	GCRminMID	GCRminBEST	GCRminLARGE
Tracer Setup	S1 and T1	S1 and T2	S1 and T3	S1 and T4

Note. SMALL/MID/BEST/LARGE denote the size of the tropospheric aerosol particles in the respective tracer setup. Likewise, we define the simulations GCRmaxSMALL/MID/BEST/LARGE.

Table 3

Simulations Conducted to Investigate the Transport and Deposition of ^{10}Be From GCR for Different Aerosol Size Distributions and Phases of the 11-Year Solar Cycle, As Well As From SEP for Different Months of the SPE Occurrence

Ensemble simulation	GCR and SPE tracers integrated	Years simulated
1...10	GCR: GCRminSMALL/MID/BEST/LARGE, GCRmaxSMALL/MID/BEST/LARGE SPE: SPE1.../12	10 years +2 spin-up years

Note. Each ensemble simulation includes all GCR and SPE tracers.

properties of the surface cover for four surface types (vegetation, bare soil, snow and water), using the big leaf approach as proposed by Wesely (1989). Note that there are some remaining difficulties in the description of deposition on snow for example, due to phoretic effects which are not explicitly included in DDEP. However, the description via bulk, empirical surface parameters should be valid on the spatial scale considered (grid points). For more information about the dry deposition parameterization also see Ganzeveld and Lelieveld (1995), Ganzeveld et al. (1998), and Kerkweg et al. (2006).

2.4. Description of Simulations

We performed passive tracer simulations with interactive chemistry switched off (EMAC in GCM mode) and prescribed preindustrial boundary conditions for greenhouse gas concentrations. Boundary conditions for ozone and sea surface temperature (SST) were prescribed as long-term climatologies from a preindustrial (PI) control simulation, representing the year 1850, with interactive ozone chemistry and ocean coupling to MPIOM (Pozzer et al., 2011). The solar forcing for the PI-run was chosen according to the recommendations of the SOLARIS-HEPPA initiative (Matthes et al., 2017).

In summary, we conducted an ensemble of 10 12-year simulations, whereby the first two years of each simulation are considered as model spin-up. Thus, a total of 100 model years have been analyzed. During each simulation, ^{10}Be is continuously produced according to the prescribed time-varying GCR production rate time series, as described in Section 2.1. As mentioned before the GCR production represents two different phases of the 11-year solar cycle: In one realization the minimum of the production rate is reached after the spin-up period (GCRmin tracers) and in the other the maximum of the production rate is reached after the spin-up period (GCRmax tracers).

Parallel to the GCR tracers (GCRminSMALL/MID/BEST/LARGE and GCRmaxSMALL/MID/BEST/LARGE) we defined individual tracers to simulate the impact of SPEs, allowing us to analyze the tracers from GCR and SEP independently. The SPE tracers were included following Spiegl et al. (2022), where the ^{10}Be tracer field, representing the SPE, is introduced on the first day of each month (i.e., 12 times) of the first model year after spin-up. The ^{10}Be tracers from the SPE are annotated according to their month of injection SPE1.../12, meaning that SPE1 is the tracer for which the SPE was initiated on 1 January, or SPE 3 is the tracer for which the SPE was initiated on 1 March, and so on. Table 3 illustrates the conducted simulations.

The SPE occurs in our simulations at different months either during the maximum phase of the decadal solar cycle (SPE1.../12 combined with GCRmin) or the minimum phase (SPE1.../12 combined with GCRmax).

The results of the analysis of the GCR tracers are presented in Section 3, while Section 4 focuses on the analysis of the SPE and its detectability.

3. Deposition Pattern of ^{10}Be Produced by GCR

The cosmogenic ^{10}Be directly produced in the troposphere as well as the ^{10}Be transported from the stratosphere to the troposphere is redistributed by convective tracer transport and mixing due to the Hadley, Ferrel and Polar cells, vertical downward transport at the HFCZ, jet streams and synoptic weather systems (Spiegl et al., 2022; Terzi & Kalinowski, 2017). The transport within the troposphere to the surface lasts on average a few days to a few weeks, depending also on the size of the coupled aerosols and thus sedimentation (Pandis et al., 1995). To be more specific, in our simulations the mean residence time in the troposphere, calculated as the time required to deposit the mean equilibrium GCR tracer concentration (deposition balances production), ranges from

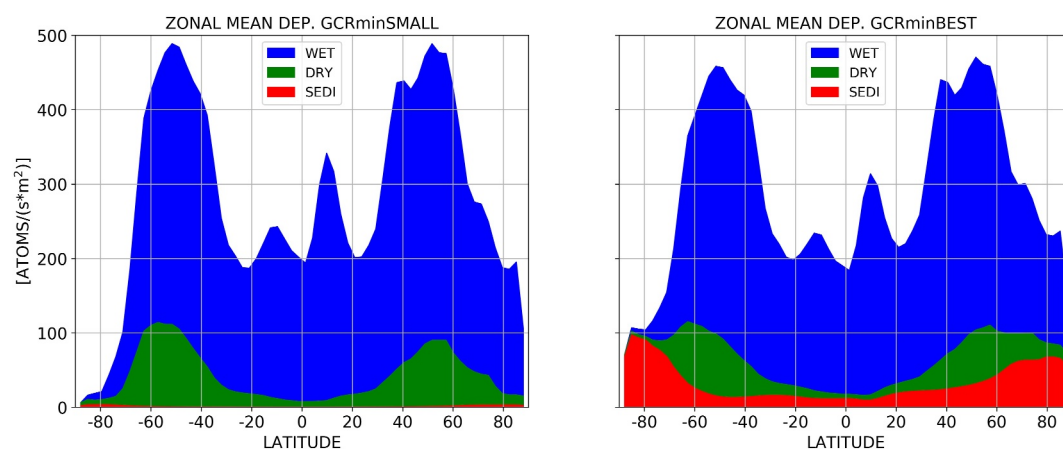


Figure 3. Zonal-mean deposition for GCRminSMALL (left) and GCRminBEST (right). The area of the color for each mechanism represents the fraction of the respective mechanism. Shown is the mean over 10 years for 10 ensemble runs (as for all following figures).

approximately 25 days for GCRminSMALL to 6 days for GCRminLARGE (GCRminMID: 16 days, GCRminBEST: 9 days).

The residence time of the cosmogenic isotopes produced in the stratosphere, however, is much longer with values between 1 and 2 years (Heikkilä et al., 2008). In our simulations for the chosen aerosol size distribution of the stratosphere S1 it is approximately 425 days. The reason why stratospheric ^{10}Be forms a long-lasting reservoir of high tracer concentrations above the tropopause is that the tropopause acts as a barrier between the stratosphere and troposphere impeding an effective and fast downward transport of ^{10}Be . In the middle atmosphere, the downward transport of ^{10}Be is determined by the seasonality of the BDC. The transport from the stratosphere to the troposphere occurs, for example, due to tropopause foldings (Spiegel et al., 2022). Note that the mean residence time for ^{10}Be from SEP with the aerosol distribution S1 is slightly longer than the residence time of ^{10}Be produced in the stratosphere by GCR (approx. 14 months). This is due to the fact that cosmogenic isotopes produced by SPEs are much more vertically distributed over the whole atmosphere than isotopes produced by GCR (compare left sides of Figures 1 and 2).

3.1. Zonal-Mean Deposition Pattern of ^{10}Be

In the following, we show the long-term annual zonal-mean deposition pattern of ^{10}Be for different aerosol size distribution setups to investigate the impact of this parameter on the deposition. In Figure 3, the three main deposition mechanisms are displayed for GCRminSMALL and GCRminBEST: wet deposition (blue), dry deposition (green) and sedimentation (red). The overall amount of deposition is the same for GCRminSMALL and GCRminBEST. However, the distribution among the different deposition mechanisms changes. Wet deposition is dominant for both, GCRminSMALL and GCRminBEST, with four local maxima, two smaller in the equatorial region as a result of high precipitation rates in the Inter-Tropical Convergence Zone (ITCZ) and two larger in the mid-latitudes. The larger maxima originate from a combination of (a) high tracer concentration in the troposphere due to tracer exchange across the tropopause for example, in tropopause folds at these latitudes (Appenzeller et al., 1996; Holton et al., 1995; Stohl et al., 2003), (b) transport in the storm track region (Wernli & Bourqui, 2002) and (c) precipitation.

The dry deposition maxima coincide with the position of the mid-latitude maxima of wet deposition, which results from the high tracer concentration at these latitudes. Note that changes in the spatial distribution of ^{10}Be production rates (e.g., due to changes of the geomagnetic field) should not qualitatively alter the deposition pattern shown in Figure 3 considerably, because atmospheric mixing is the most important factor controlling the ^{10}Be deposition pattern (Heikkilä et al., 2013).

The most notable difference between the two deposition patterns is the contribution of sedimentation, particularly in the polar regions. For GCRminSMALL, that is, the same aerosol size distribution in the troposphere as in the stratosphere (see GCRminSMALL in Table 1: S1 and T1), the surface flux due to sedimentation is rather weak,

especially in the Antarctic region. In contrast, if considerably bigger aerosol sizes are considered in the troposphere (see GCRminBEST in Table 1: S1 and T3), sedimentation becomes the dominant deposition mechanism at high latitudes, particularly over Antarctica, and a steady deposition background for all other latitudes. The reason for the increase of the deposition at high latitudes, especially southwards of 80°S, is that in the BEST scenario ^{10}Be produced in the troposphere (37% see right side of Figure 1) is deposited much closer to the places where it was produced than in the SMALL scenario, where some of the ^{10}Be is transported on longer trajectories to latitudes away from the location of production (see also the different mean residence time in the troposphere of the two scenarios mentioned before). Consequently, the maxima in the distribution of the SMALL scenario are increased compared to the BEST scenario, because the overall deposition is the same for both distribution (but distributed differently) and longer trajectories are more likely to end in the maxima.

To illustrate the seasonal variations of the zonal-mean deposition, Figure 4 shows the seasonal interplay of tracer transport, convective and large-scale precipitation and deposition. The uppermost panel depicts the anomalies of the monthly zonal-mean amount fraction of ^{10}Be versus the long-term yearly zonal-mean over pressure (for GCRminBEST).

The absolute amount fraction of ^{10}Be is highest in the stratosphere, where the majority of ^{10}Be is produced by GCR and vertical tracer exchange to the troposphere is limited. The seasonal change of the amount fraction in panels (a), especially in the polar region, results from the BDC. In NH winter, the BDC transports large amounts of ^{10}Be toward the North Pole, leading to high amount fraction anomalies in January to May above that pole. In NH summer, stratospheric ^{10}Be is transported to the South Pole, increasing the amount there in July to September. The panels (b) below show the anomalies of the tracer amount at 544 hPa, which represents the amount of tracer that is introduced from the stratosphere to the troposphere due to STE plus tropospheric background concentration, so the amount of the tracer which is available for tropospheric downward transport and deposition. The positive near-ground (around 1000 hPa in (a)) anomalies of the NH are in March and May, whereas the maxima for the SH are mainly in July (near the equator) and September. The zonal-mean precipitation shown in panels (c) shows the seasonality of precipitation, for example, the shifting equatorial maxima caused by the motion of the ITCZ. The equatorial convective precipitation maxima (light-green color in panels (c)) directly correlate with the zonal-mean equatorial wet deposition maxima of ^{10}Be due to washout, that is, impact scavenging. The blue shaded area in panels (d) shows the maxima of convective aerosol wet deposition.

In the mid-latitudes, convective precipitation leads to seasonally occurring peaks from impact scavenging, for example, in the NH in January/March around 35°–40°N. The zonal-mean large-scale precipitation (light-blue color in panel (c)) has less pronounced seasonal variability than the convective precipitation in the ITCZ, but, due to the varying tracer amount caused by STE and horizontal transport in the troposphere, the wet deposition of ^{10}Be due to large-scale precipitation changes considerably over the year (see large-scale aerosol wet deposition shown by the dark blue color in panels (d)). The overall maximum of wet deposition in the NH appears in May, where almost no convective precipitation is present, but the large amount of tracer leads to nucleation scavenging and downward transport from large-scale precipitation. The overall maximum of wet deposition in the SH appears in September to November (70°–30°S).

To further quantify the relevance of different deposition mechanisms, their seasonality and differences between different aerosol setups (here GCRminSMALL and GCRminBEST), Figure 5 shows the zonal-mean ratio of each individual deposition mechanism to the sum of all deposition mechanisms over the four seasons for GCRminSMALL and GCRminBEST. The most significant difference between GCRminSMALL and GCRminBEST over the year appears in the polar regions. For GCRminSMALL in the southern polar region, dry deposition is stronger than sedimentation, whereas for GCRminBEST, sedimentation is almost the only relevant deposition mechanism throughout the whole year in that region.

Wet deposition, which is the dominant deposition mechanism in the mid-latitudes and equatorial region, drops for GCRminBEST below 50° south of 65°S and for GCRminSMALL south of 80°S. In the northern polar region, GCRminBEST shows a pronounced seasonal march, with a drop of the ratio of wet deposition below the ratio of sedimentation in the winter months December, January and February, showing that the large sedimentation in the Arctic depicted in Figure 3 is mainly a result of increased sedimentation in NH winter. Moreover, dry deposition is increased during this time span because both mechanisms correlate with high tracer concentrations near the surface coming from increased downward tracer transport and the absence of precipitation in that period (see also Figures 4a and 4b for January). For GCRminSMALL the seasonal evolution is qualitatively similar, but less

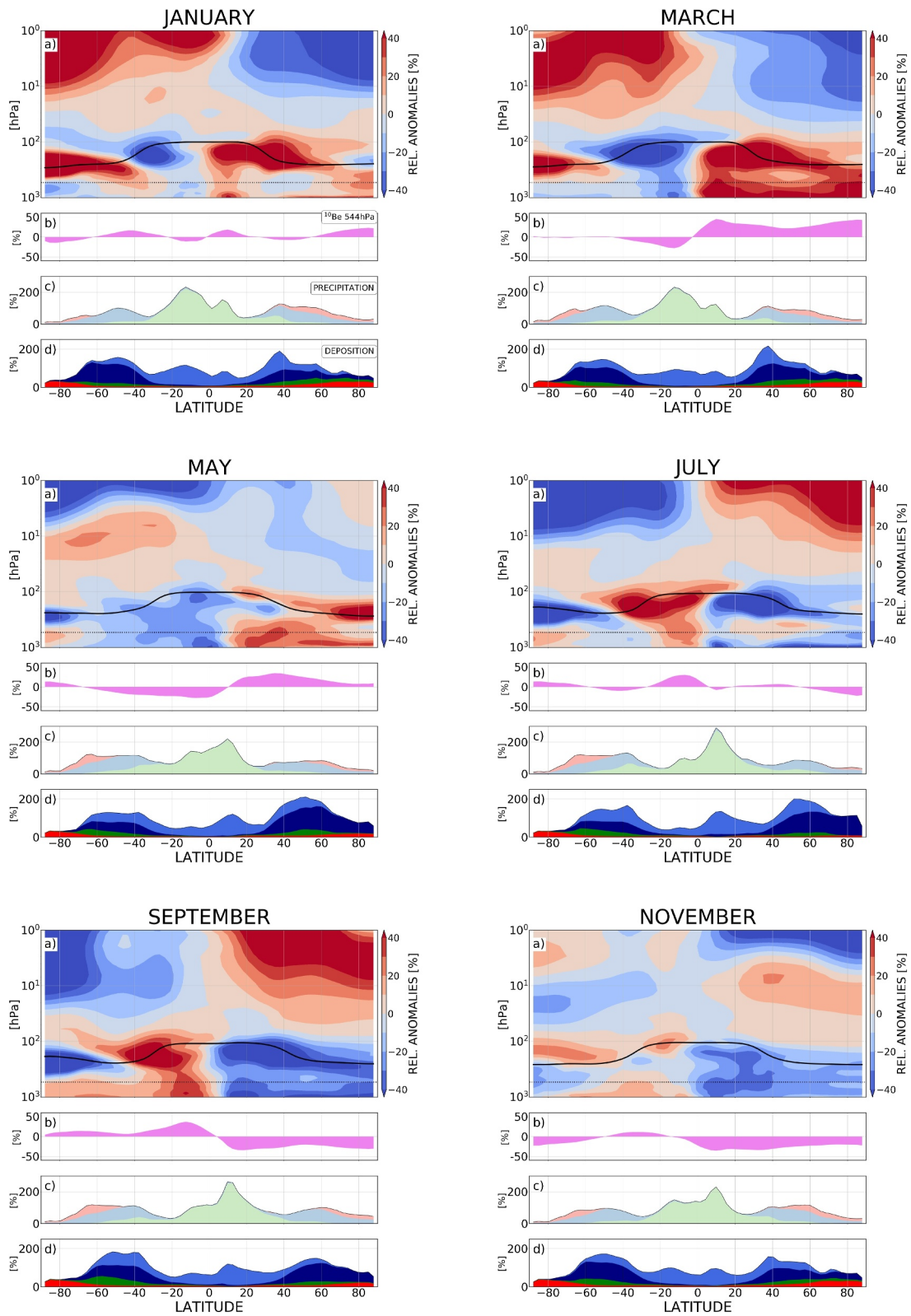


Figure 4.

pronounced, with wet deposition being the dominant deposition mechanism throughout the whole year (except for very high southern latitudes, especially in NH summer and autumn).

In the following figures (if not stated otherwise), we consider GCRminBEST only, because this combination of aerosol particle size distributions for the stratosphere and troposphere is reasonable for both hemispheres (see e.g., Deshler, 2008; Malinina et al., 2018; Pandis et al., 1995) and gives a total deposition flux of around 100 atoms/(m²s) at different drilling sites as shown in Table 4, which is similar to the background of the CE 774/775 SPE (ice core data column Table 4), the approximated empirical background in Spiegl et al. (2022) and other studies by Mekhaldi et al. (2015) or Sukhodolov et al. (2017) at these locations. The locations are drilling sites, where ¹⁰Be ice core data was measured in Greenland from the North Greenland Ice core Project (NGRIP) and the North Greenland Eemian Ice Drilling (NEEM), as well as in Antarctica from Dome Fuji and the West Antarctic Ice Sheet Divide Core (WDC).

GCRminSMALL and GCRminMID underestimate the total deposition flux near the drilling sites, while GCRminLARGE slightly overestimates the total deposition flux at these locations and generally overstates the role of sedimentation in other latitudes (not shown). This qualitatively applies also to the GCRmax tracers (not shown). Accordingly, GCRminBEST (GCRmaxBEST) gives the best results in comparison to empirical data of the ice cores, as shown in detail in Section 4.

3.2. Global Deposition Pattern of ¹⁰Be

To further improve the understanding of the surface deposition of ¹⁰Be, we now analyze the mean deposition patterns as a function of latitude and longitude. Figure 6 shows the total long-term annual-mean global deposition pattern (DEP. ALL) (top left) and global patterns of wet deposition (DEP. WET), dry deposition (DEP. DRY) and sedimentation (DEP. SEDI).

Areas of high surface deposition rates are mostly confined to the tropics and the storm track regions of the NH and SH, with local maxima over the North Atlantic south of Greenland, over the North Pacific between Canada and Russia, and the Southern Ocean surrounding Antarctica. The total deposition pattern shown in Figure 6 is comparable to results for the total ¹⁰Be deposition flux shown in Field et al. (2006) and Heikkilä et al. (2013), but with some deviation due to differences in the modeling approach and parameter settings (see Section 1). The deposition patterns of the different deposition mechanisms are addressed in more detail in the following to work out the relation between the local tracer amount, precipitation, surface properties, wind speed and sphere of production (troposphere or stratosphere).

The amount of ¹⁰Be in the mid-troposphere at 544 hPa (Figure 7, row 1) is influenced by both the seasonality of STE as well as tropospheric dynamics, and represents the amount of tracer, which then becomes available for further synoptic dynamics and transport in the troposphere below, nucleation scavenging and impact scavenging due to precipitation. During the boreal spring season in March, highest concentrations of ¹⁰Be in 544 hPa occur at NH subpolar latitudes as a result of a particularly strong downward transport from the middle atmosphere to the troposphere (compare Figure 4).

In contrast, the SH polar latitudes depict highest tracer concentrations in January, and thus not before the austral summer season, which can be attributed to an overall slower downward progression of the material during the SH dynamical active period (Spiegl et al., 2022). Regions with high precipitation, especially in the tropics (see Figure 7, row 2), are dominated by wet deposition since impact scavenging (washout by rain droplets) deposits large amounts of ¹⁰Be at the surface. However, the overall wet deposition pattern is influenced by both the seasonal cycle of precipitation (sink) and the tracer supply from the stratosphere (source), which is higher in the middle to high latitudes than in the tropics. In this context, the absolute maxima of wet deposition in the NH long-term annual-mean zonal-mean (compare Figure 3) is shaped by a complex interplay of different mechanisms at distinct geographic locations and seasons. Examples are the intense wet deposition south of Greenland in January

Figure 4. (a) Relative anomalies of long-term monthly zonal-mean amount fraction vs. long-term yearly zonal-mean of ¹⁰Be over pressure for GCRminBEST. The black line shows the tropopause and the dotted line the position of the 544 hPa pressure level. (b) ¹⁰Be amount relative to long-term yearly zonal-mean for each latitude at 544 hPa. (c) Zonal-mean precipitation relative to average over all latitudes: light green—convective precipitation, light blue—large scale precipitation, light red—snow fall. (d) Monthly zonal-mean deposition pattern for GCRminBEST relative to average over all latitudes (colors like in Figure 3, but wet deposition separated into convective (blue) and large scale (dark blue) aerosol deposition).

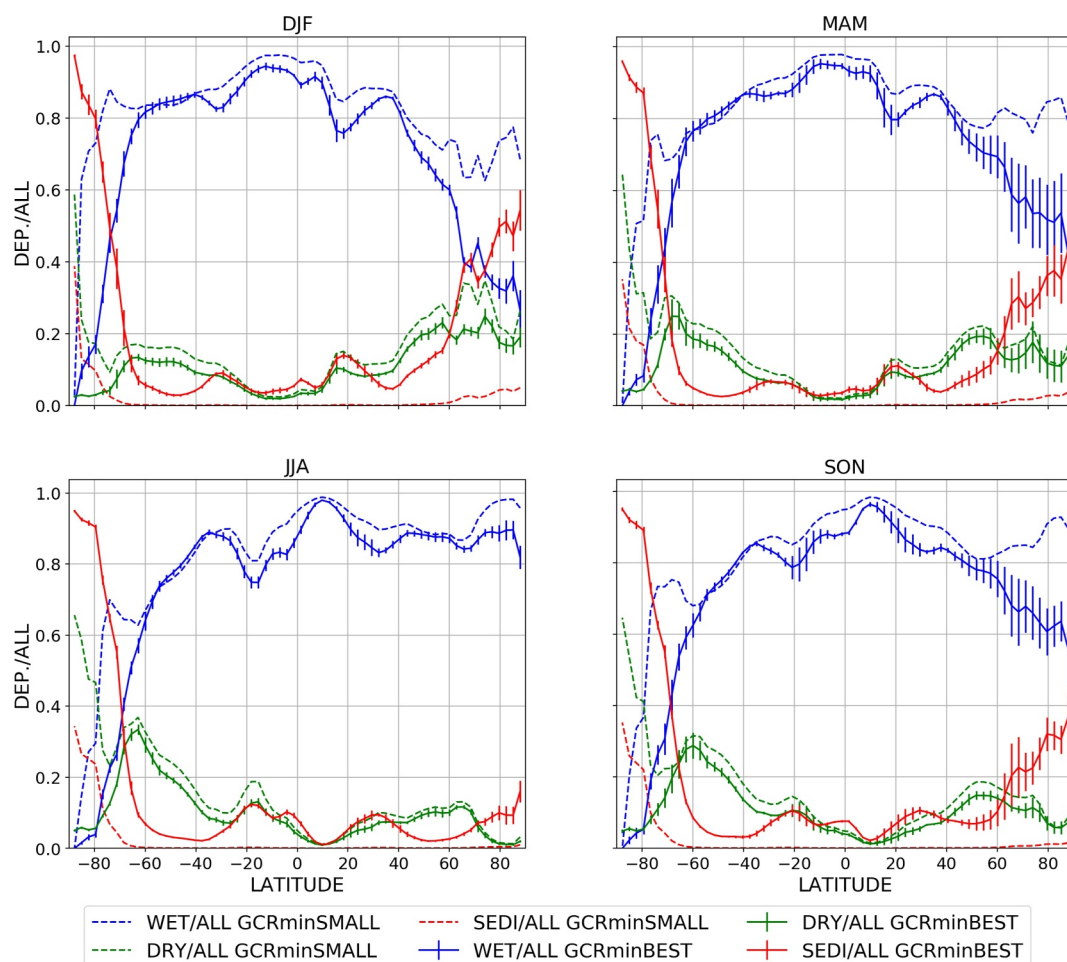


Figure 5. Ratio of the seasonal zonal-mean deposition as a function of latitude for wet deposition, dry deposition and sedimentation (dashed line: GCRminSMALL; solid line: GCRminBEST). The error bars indicate the standard deviation (only for GCRminBEST). DJF means December, January, February etc.

and March due to large-scale precipitation and high synoptic activity, and the high wet deposition over Siberia and Canada in July (see Figure 7, row 3). The absolute maxima of wet deposition in the SH, shown in Figure 3, result from a large band of wet deposition surrounding the Antarctic continent that shows less seasonal variability than its counterpart in the NH (compare Figures 3 and 4).

Table 4

Long-Term Annual Mean and Standard Deviation of ^{10}Be Deposition Flux [$\text{Atoms}/(\text{m}^2\text{s})$] for GCRmin Tracers for the Locations of Two Different Drilling Sites in Greenland (NGRIP and NEEM) and Two in Antarctica (Dome Fuji and WDC)

	GCRminSMALL	GCRminMID	GCRminBEST	GCRminLARGE	Ice core data
NGRIP	26.5 ± 12.5	31.2 ± 11.9	92.1 ± 16.7	110.5 ± 13.1	98.2 ± 12.8
NEEM	29.8 ± 16.6	30.3 ± 14.6	79.8 ± 13.4	104.7 ± 14.1	90.2 ± 15.5
Dome Fuji	11.2 ± 2.7	24.2 ± 3.8	108.1 ± 12.1	122.7 ± 12.0	86.1 ± 11.3
WDC	38.4 ± 12.4	43.2 ± 11.8	117.3 ± 13.4	145.2 ± 13.1	105.4 ± 14.9

Note. Note that the standard deviation for NGRIP, NEEM and WDC stays in the same range, because it is controlled by precipitation (wet deposition), while for Dome Fuji the variability changes with increased sedimentation flux. The values of the ice core data column are calculated from the ice core data for the CE 774/775 SPE, after the SPE has decayed (+5 years after the SPE, see Figures 10 and 11).

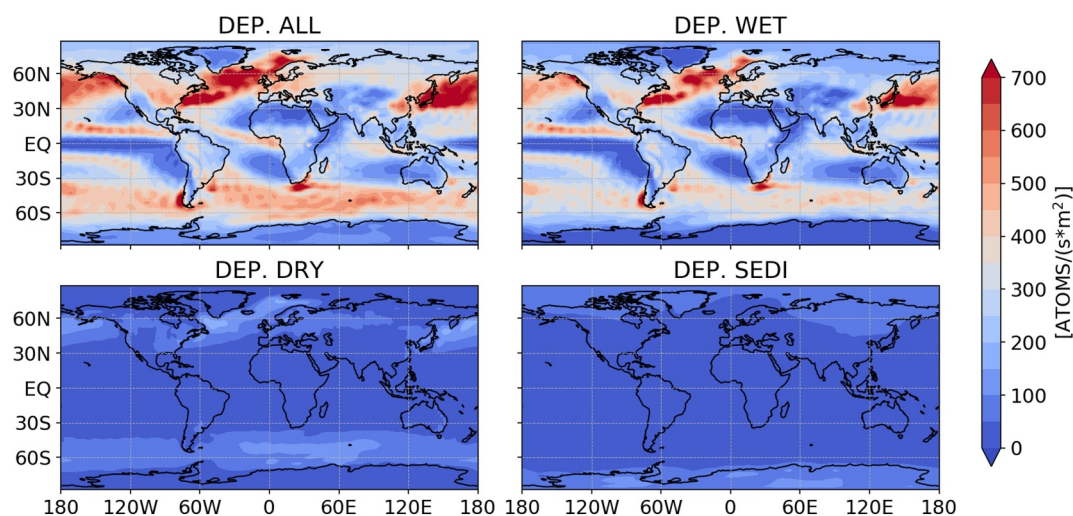


Figure 6. Mean global deposition pattern for all deposition mechanisms combined (top left), wet deposition (top right), dry deposition (bottom left) and sedimentation (bottom right) for GCRminBEST.

The Pearson correlation between the wet deposition and precipitation (sum of large-scale and convective precipitation and snowfall), shown in Figure 7 (row 4), is constant throughout the whole year, with a long-term global-mean value of around 0.6 ($P \ll 0.05$), which means that 36% of the variation of the wet deposition comes from changes in precipitation alone. For the Antarctic and the polar regions of the NH, areas of rather weak correlations are found, for example, for January, March and September. These weak correlations have two major reasons: (a) When the precipitation is low but the tracer concentration is high inside a cloudy atmospheric layer, nucleation scavenging (droplet growth and subsequent in-cloud scavenging) dominates the wet deposition pattern without the need of rainfall. (b) When the precipitation is high and tracer concentration is low, situations occur when a lot of rainfall will not automatically lead to pronounced wet deposition at the surface, for example, in the tropics. Both points inhibit high correlations between wet deposition and precipitation.

Figure 8 depicts the dry deposition shaped by an interplay of near surface wind (10 m wind speed) and the seasonality of the surface friction characterized by changes of the leaf area index. The leaf area index is controlled by the phenological cycle and thus vegetation cover. During seasons of high vegetation cover, the leaf area index is higher and surface friction is more intense, which increases near surface turbulence and thus dry deposition. The patches of dry deposition over land in the NH in July, for example, are mainly driven by a peak of the phenological cycle during that time. However, the most important parameter of the dry deposition in our simulations is the horizontal wind speed close to the surface, that is especially intensified in regions of high synoptic activity with flat topography over the open ocean, leading to large areas of pronounced dry deposition south of Greenland and between Alaska and Japan (in January/March) as well as north of Antarctica (in July/September).

The global mean value of the Pearson correlation between the 10 m wind speed and the dry deposition is seasonally almost constant with a value of 0.6 ($P \ll 0.05$) and thus as high as the correlation between precipitation and wet deposition, which means (in a global picture) that the 10 m wind speed is as good as an indicator for dry deposition as precipitation is for wet deposition. In areas, where the near-surface wind speed is low compared to its global mean, and other factors such as the surface properties (e.g., due to changes of the leaf area index) become more important for dry deposition, correlations between the 10 m wind speed and dry deposition drop. Also, if other deposition mechanisms, such as wet deposition, reduce the amount of tracer available for dry deposition and wind speed is high, the correlation can be negative. This occurs mainly in the western part of Antarctica during March, July and September.

As shown in Figure 9, the global surface flux from sedimentation results almost entirely (>95%) from the deposition of ^{10}Be produced in the troposphere for both the NH and SH. The global ratio of the deposition due to sedimentation from tracer being produced in the troposphere is 97.5%. The reason for this is the difference in aerosol size distribution between the troposphere (mean radius 0.6 μm , and standard deviation 2.0) and the stratosphere (mean radius 0.1 μm , and standard deviation 1.4) for GCRminBEST.

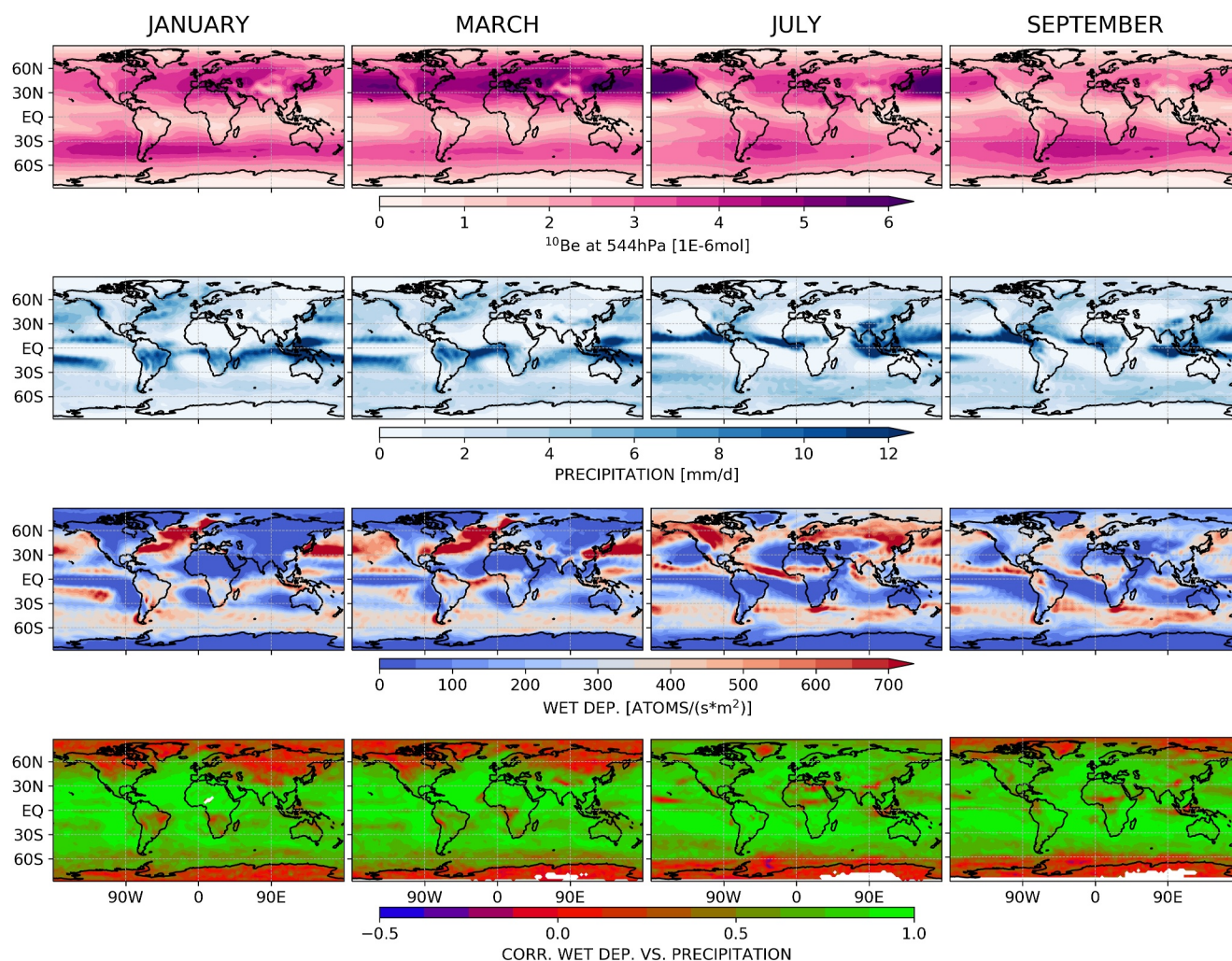


Figure 7. Row 1: 10-year monthly-mean ensemble-mean for ^{10}Be in 544 hPa. Row 2: global precipitation (convective, large-scale precipitation and snowfall). Row 3: global wet deposition pattern. All depicted for 4 different months, representing different seasons of the year (GCRminBEST). Row 4: Pearson correlation between wet deposition and precipitation (white patches occur in regions of no or extremely low precipitation).

For GCRminSMALL, where the aerosol size distribution of the troposphere and stratosphere are equal, the fraction of deposition due to sedimentation of isotopes produced in the troposphere or stratosphere corresponds directly to the amount of particles being produced by GCR in the respective sphere (stratosphere approx. 65% and troposphere approx. 35%, not shown). Note that for GCRminBEST the deposition due to sedimentation is a factor 35 higher than for GCRminSMALL. The drop of the sedimentation flux in NH summer (April to October) shown in Figure 9 results from lower tracer concentrations near the surface due to the wash out of ^{10}Be by wet deposition in that season and less STE (see also Figures 4 and 5). Note that the sedimentation flux during the drop comes entirely from ^{10}Be produced in the troposphere. The fraction of stratospheric ^{10}Be here is almost zero. The sedimentation flux in the SH shows only slight variations with a small increase from September to November, resulting from an increase of tracer concentration due to the seasonality of the BDC (compare Figure 4). Here, the amount of sedimentation from ^{10}Be produced in the stratosphere slightly increases for the maxima.

4. Detectability of SPEs in ^{10}Be Ice Core Data

Similar to Spiegl et al. (2022), we compare our simulations to ice core data covering the CE 774/775 SPE, this time, however, including also a simulated, time-varying GCR background, as shown in Figure 10. For all drilling sites considered, NGRIP and NEEM in Greenland, as well as Dome Fuji and WDC in Antarctica, we find very good agreement for both the GCR background and the peak due to the SPE. (Additional information on the data

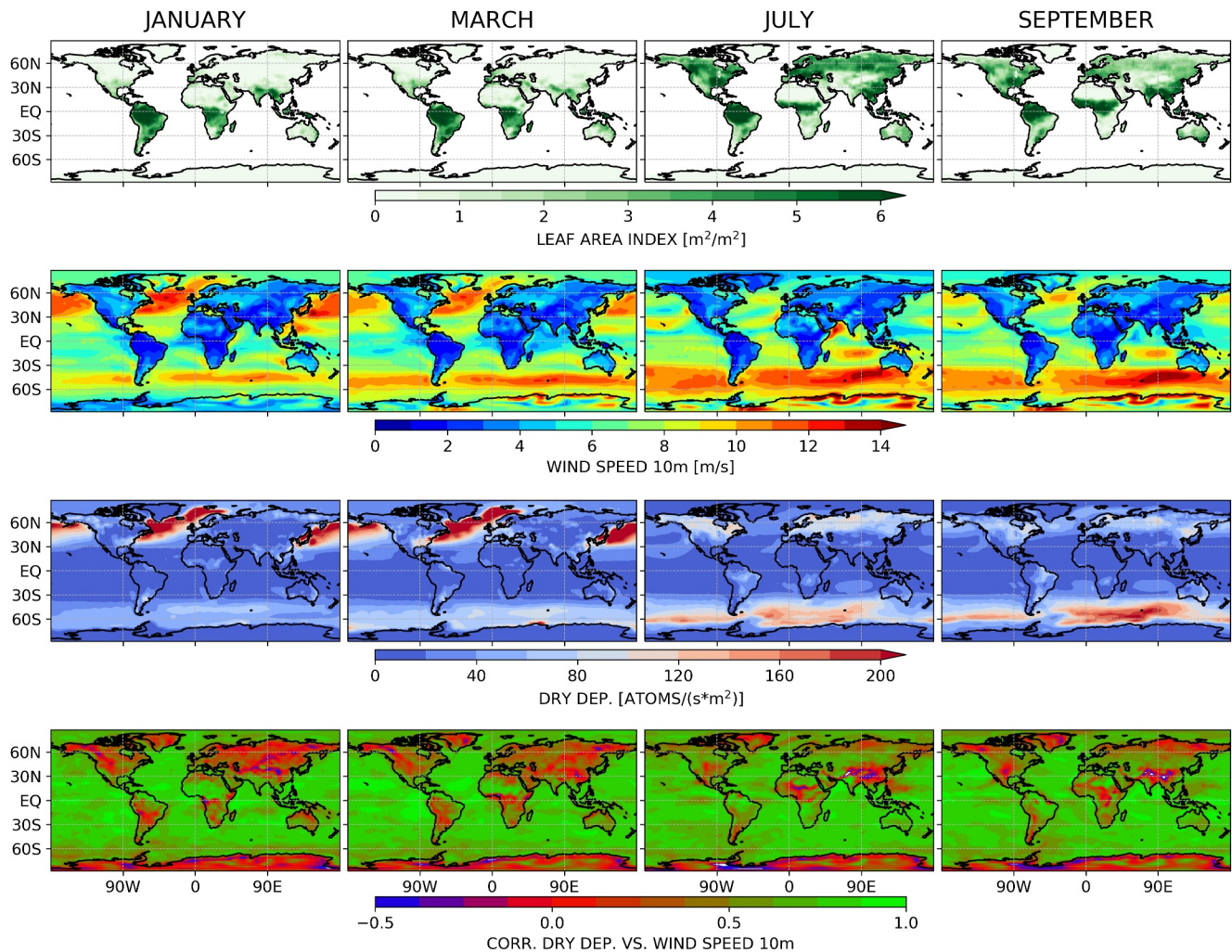


Figure 8. Row 1: 10-year monthly-mean ensemble-mean for the leaf area index. Row 2: 10 m horizontal wind speed. Row 3: global dry deposition pattern. All depicted for four different months, representing different seasons of the year (GCRminBEST). Row 4: Pearson correlation between dry deposition and 10 m horizontal wind speed.

sets are provided by Mekhaldi et al. (2015) and Sigl et al. (2015), and for the Dome Fuji data set by Miyake et al. (2015)).

Figure 10a shows the amount ratio of ^{10}Be , produced by the CE 774/775 SPE and GCR, over time above the respective NH location. With the small periodic drops of the height of the tropopause in winter and spring, tracer is transported from the stratosphere to the troposphere, leading to small maxima in dry deposition and sedimentation, followed by increased wet deposition due to precipitation and nucleation scavenging in NH summertime, shown in Figure 10b. This is repeated in an annual cycle with decreasing amplitude, until the GCR-background surface flux of ^{10}Be is met again. Depending on the season in which the SPE occurs, the position of the annual mean peak of the surface flux in a yearly resolution (which is the given resolution of the ice core data) can differ. For SPE1, SPE4 and SPE7 (initialization at the first of January, April and July) the peak in the yearly data occurs within the first year of the SPE, because the cosmogenic isotopes produced are almost directly transported to the troposphere and deposited. If the season of the injection of ^{10}Be from the SPE coincides with a phase of increased precipitation in the first year, the peak will be increased, as it is the case for SPE7 compared to the other SPE injection times at NGRIP. For the SPE that occurs later in the year, as it is the case for SPE10, the peak can be shifted to the next year, since most of the additional ^{10}Be from the SPE in the stratospheric reservoir is introduced to the troposphere in winter and spring of the next year.

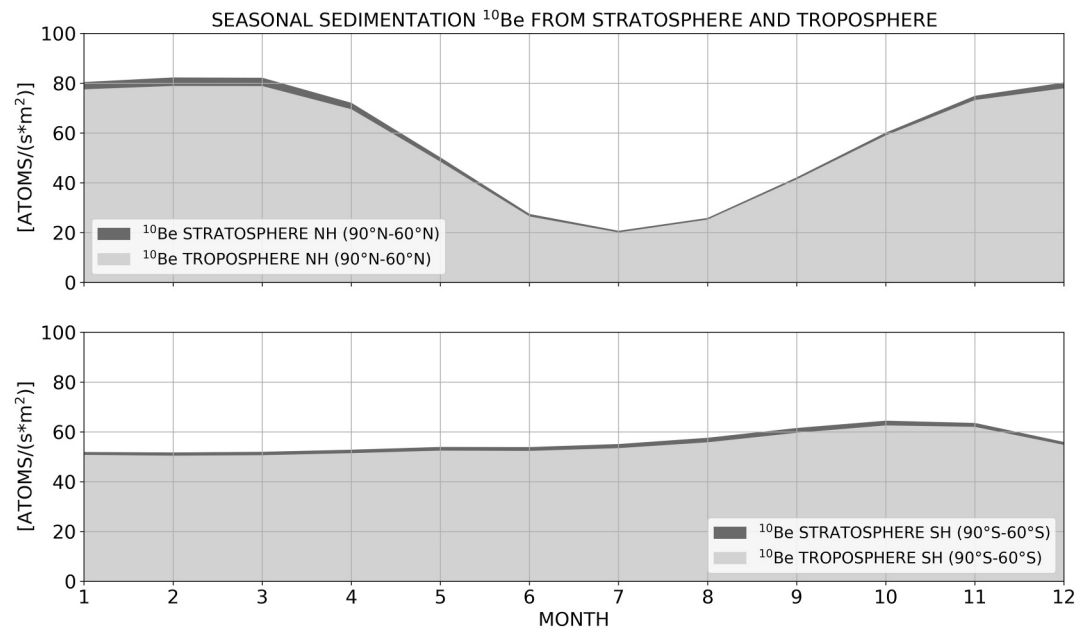


Figure 9. Annual cycle of the global-mean long-term sedimentation surface flux for the NH (90°–60°N) and SH (90°–60°S) for GCRminBEST. Light gray and dark gray represent the sedimentation of ^{10}Be produced in the troposphere and in the stratosphere.

Note that the measured ice core data is shifted in a way to fit the peak within the first year but could also be shifted such that the peak fits the peak of for example, SPE10, meaning that the position of the peak does not indicate a specific season in which the SPE occurred (for yearly resolution). However, the slope of the curve could indicate a season of occurrence, since the peak of SPE10 is less pronounced and broader than the peaks of SPE1/4/7 (Figure 10c). Furthermore, we notice only small differences between GCRminBEST (solid line) and GCRmaxBEST (dashed line), so the phase of the 11-year solar cycle which the SPE meets, has no strong impact on the surface flux in ice core data at the considered locations in Greenland.

Note also that the ^{10}Be from SEP is deposited almost only by dry and wet precipitation, while for the ^{10}Be from GCR the majority goes to sedimentation. The reason for this is that ^{10}Be from GCR is produced to a large amount in the troposphere (>35%, see Figure 1) where it couples to larger aerosols (T3 in Table 1 for BEST-Scenario) than the stratospheric aerosols to which the ^{10}Be from the SEP couples (S1). However, this only affects the deposition pattern at high latitudes, as the comparison of GCRminBEST and GCRminSMALL (S1 + T1, S1 = T1, Table 2) in Figure 3 shows. Also, the global deposition pattern of ^{10}Be from GCR (Figure 6) and SEP (not shown) are qualitatively similar.

Figure 11 shows the same quantities as Figure 10, however, for the Dome Fuji and WDC ice cores in Antarctica, where the annual cycle in tropopause height is more pronounced than in the Arctic. For WDC, SPE1 gives the best overlap with the data. Also, SPE4/7/10 show good agreement, but with a less pronounced peak. Compared to NGRIP and NEEM in the NH polar regions, WDC shows more continuous wet deposition with a less pronounced seasonal amplitude (Figure 11b) for WDC. At Dome Fuji, however, almost no wet deposition is present due to the lack of precipitation in that area, which also leads to a much less pronounced imprint of the SPE compared to the data from the other ice cores.

Note that it might be also possible to derive ^{10}Be concentrations in ice core layers from precipitation results for the respective drilling sites. However, this requires additional ice-core layer models for the simulation of the redistribution of ^{10}Be inside the ice, which are not included in our model. Further note that the model shows a longer decay of the SPE signal in comparison to measurements for all four drilling sites. A reason for this could be that in the simulation the ^{10}Be from the SPE couples only to small stratospheric aerosols, whereas in reality also some larger tropospheric aerosols might be involved in the transport and deposition. Therefore, the decay in the model is a bit longer than in the ice core data. Another difference is that the variability of the measurements is

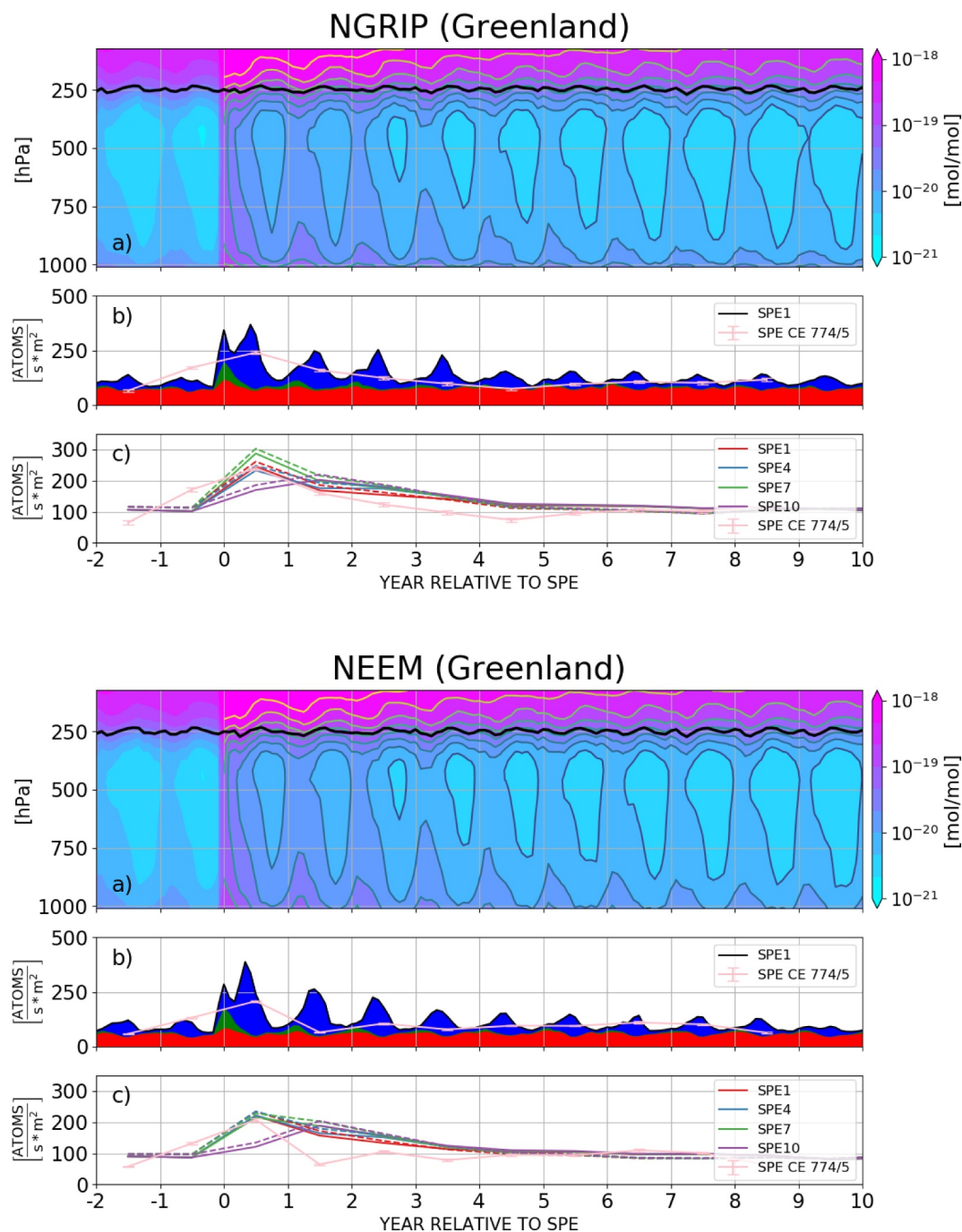


Figure 10. Comparison of the simulated ^{10}Be flux to ice core data from Greenland (NGRIP and NEEM). (a) Modeled ^{10}Be amount ratio as a function of height and time in the troposphere and lowermost stratosphere (black line: tropopause, shown for GCRminBEST, contour lines start after SPE), (b) the ^{10}Be surface deposition from different mechanisms (blue: wet deposition, green: dry deposition, red: sedimentation), and (c) the annual ^{10}Be amount compared to the ice core data (pink line). The solid lines show the results for SPE1/4/7/10 combined with GCRminBEST, and the dashed lines show the results for SPE1/4/7/10 combined with GCRmaxBEST, where GCR is in the maximum phase when the SPE is introduced. The modeling results show area means of grid points surrounding the drilling site of the ice cores.

larger than the variability of the model, because the measurements represent a specific location (the drilling site), whereas the model results show the mean of all ensemble simulations for a larger area (grid points). Both factors potentially lead to a smoothing of the variability seen in the ice core data. Comparing our results to our former

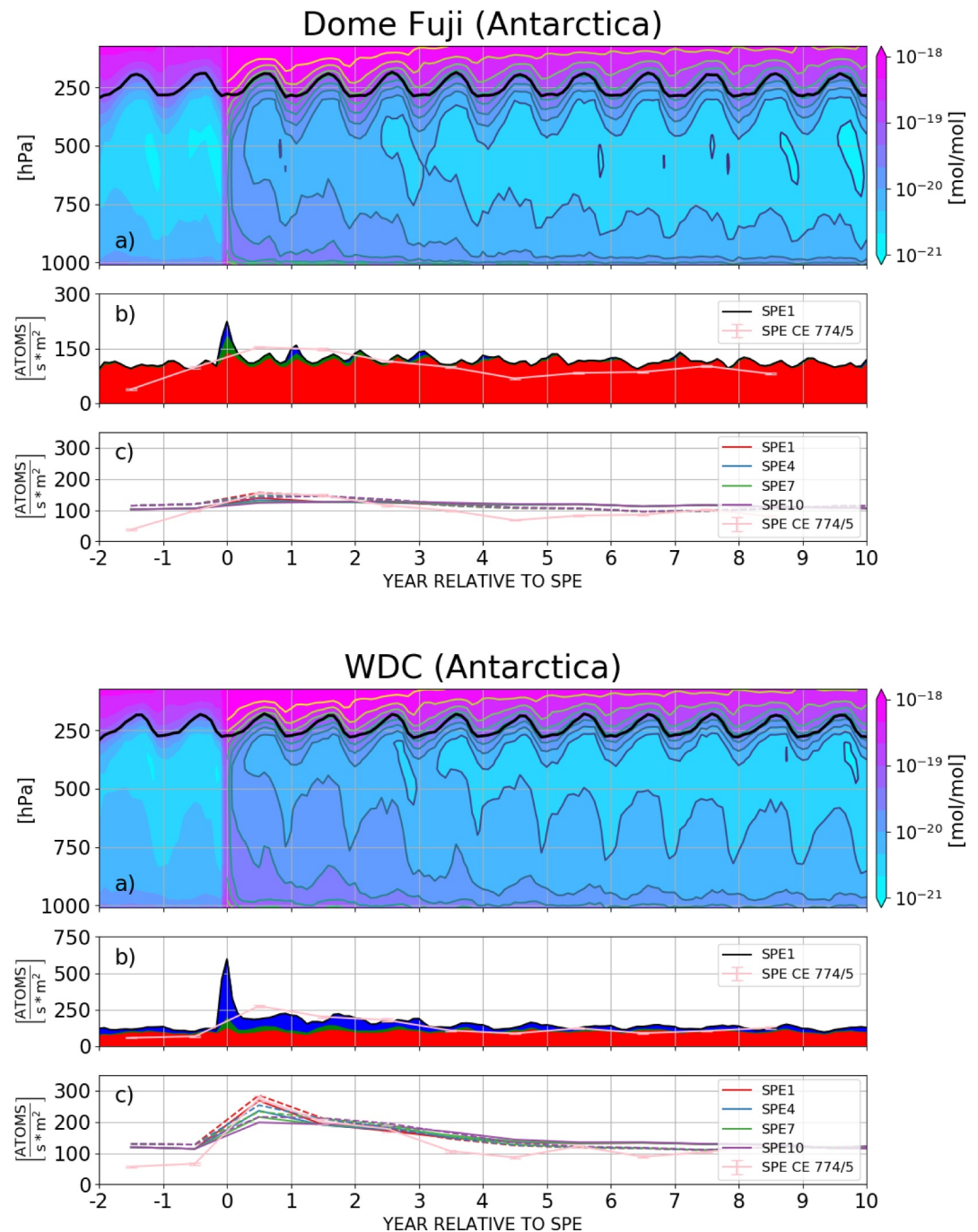


Figure 11. Same as Figure 10, but for the Dome Fuji and WDC ice cores (Antarctica).

paper Spiegl et al. (2022), the signal of the SPE at the drilling sites has decreased, considering the higher scaling factor of the SPE in this paper. The reason for this is a combination of the introduction of nucleation scavenging, which additionally deposits ^{10}Be introduced to the troposphere at mid-latitudes before it can be transported to higher latitudes, and the higher standard deviation of the size distribution of the stratospheric aerosols used in Spiegl et al. (2022).

Based on our SPE sensitivity studies, we found that the in situ state of the middle atmosphere during the injection month as well as the tropospheric precipitation regime both modulate the signatures of cosmogenic nuclides at different locations, in agreement with Spiegl et al. (2022). This also partly applies to the respective phase of the

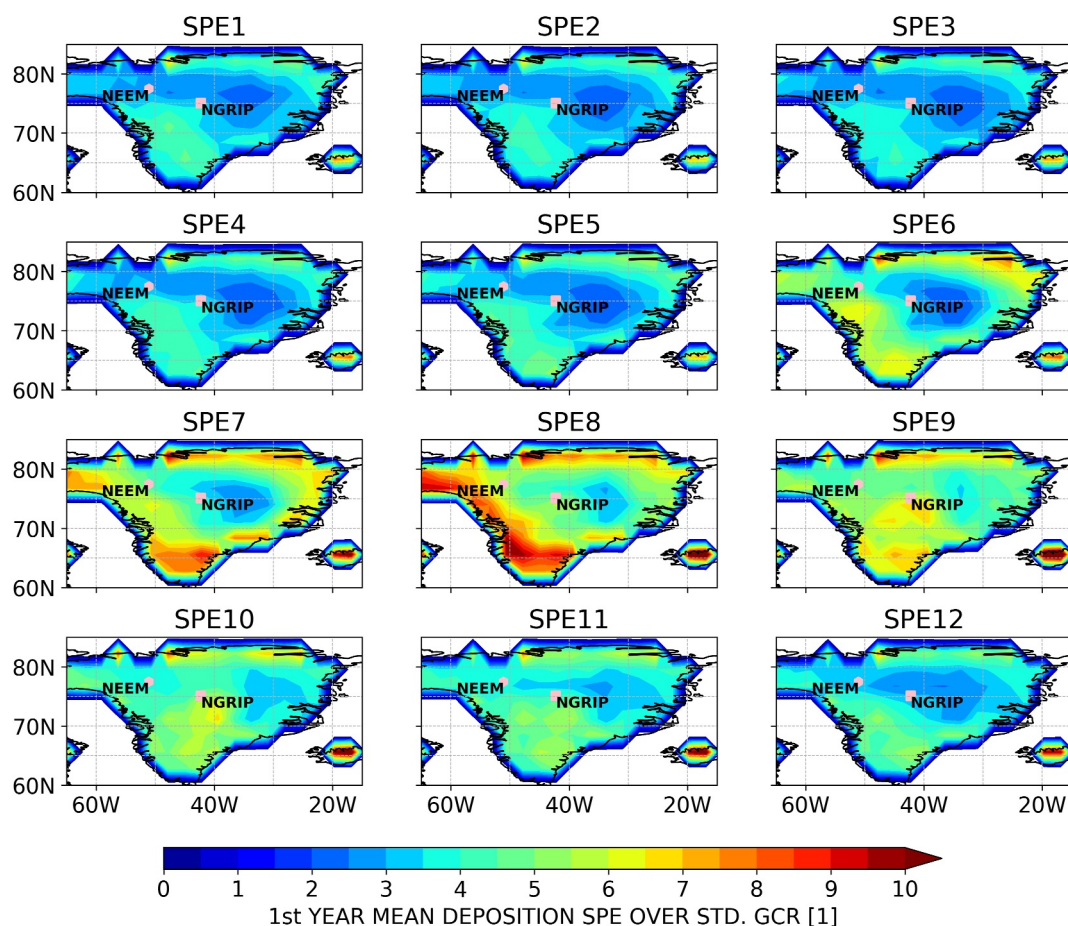


Figure 12. First year mean deposition of SPE produced ^{10}Be for Greenland in units of the standard deviation of GCR for SPE1 to SPE12 and GCRminBEST background. SPE1 to SPE12 denotes the initialization month of the SPE (SPE1—January, SPE2—February etc.).

solar cycle. From our results we infer that the detectability of an SPE in natural archives of ^{10}Be is suspected to change as a consequence of modulating parameters. In the following, we present a novel analysis that estimates the detectability of an SPE compared to GCR background in dependence of the location, the season at which the SPE occurs, the phase of the 11-year solar cycle the SPE meets, and the size distribution of the aerosols to which the ^{10}Be couple for Greenland and Antarctica.

To derive the detectability of an SPE in ice core data of ^{10}Be , we calculate the ratio of the mean deposition of the respective SPE within the first year after its occurrence (signal) and the standard deviation of the annual deposition of ^{10}Be from GCR (background). This is a typical signal to noise measure but can also be interpreted as the inverse coefficient of variance between the SPE and the GCR produced ^{10}Be , as a metric for the detectability of the SPE. If the coefficient is much larger than one, the SPE should be easily detectable at the specific location where the ice core was taken, because the amount of ^{10}Be produced by the SPE deposited in that location is large compared to the variability of the GCR produced. If the coefficient falls below a certain threshold (typically 2–3 standard deviations of the background signal, depending on the experimental setting and the additional information given), the SPE is likely to not be detected in the respective ice core data.

Figure 12 shows the detectability of SPE1 to SPE12 in Greenland for the GCRminBEST background and the CE 774/775 SPE. The detectability of an SPE of the same order at NEEM is in general slightly higher than at NGRIP, because NGRIP is located at the border of an area east of NGRIP where low precipitation rates lead to a weaker SPE related deposition signal within the first year but with a similar GCR related noise (standard deviation) compared to NEEM. However, it should be noted that Figure 12 shows the results of an ensemble mean. The detectability at NGRIP can vary for a single realization considerably due to its position close to the low

detectability area and seasonal variability, for example, for an SPE occurring in September or October (SPE9 and SPE10) the detectability at NGRIP could overcome the detectability at NEEM.

Based on Figure 12, it appears to be possible to suggest or reject positions of possible drilling sites. For example, a drilling site directly inside the low detectability area east of NGRIP might be a less useful choice for the detection of SPEs, whereas a drilling site close to NEEM or even south of NEEM, within the area of maximum detectability for SPE7 and SPE8, would allow also the detection of an SPE in ice cores that could not be detected in other areas of Greenland.

Figure 13 shows the detectability of SPE1 to SPE12 in Antarctica, which is in general comparable to the detectability of SPEs in Greenland but with more pronounced differences between the very dry region surrounding Dome Fuji and the area of high detectability close to WDC. The detectability shows less pronounced variability throughout the year at the drilling sites WDC and Dome Fuji compared to Greenland.

Figure 14 shows the detectability at NGRIP, NEEM, Dome Fuji and WDC for four different tracer settings, GCRminSMALL/BEST, where the SPE coincides with the minimum phase of GCR production related to the maximum of the 11-year solar cycle, and vice versa for GCRmaxSMALL/BEST. The different settings show considerable differences with respect to the regional detectability. For NGRIP the seasonal variability of the detectability is more pronounced than for NEEM, as already suggested in Figure 12. The particular months of introduction of the SPE to the model, with highest detectability are September to October (SPE9/10) for NGRIP and June and July (SPE6/7) for NEEM. This means that SPEs occurring in these months might be detected, whereas an SPE of the same magnitude occurring in other months could not be detected anymore.

Büntgen et al. (2018) estimated from ^{14}C data that the CE 774/775 SPE occurred during the boreal tree growing season in June to August. Further, an SPE coinciding with the maximum phase of GCR production is, in general, harder to detect than an SPE occurring during the minimum phase of ^{10}Be production by GCR. This is of interest, because the relative variability of ^{10}Be from GCR is higher within the GCRmin phase according to the higher variability of the production rate (see Section 1 and Figure 1). However, for the maximum phase of production the general amount of deposition due to GCR produced ^{10}Be is much larger, and thus also the absolute values of its standard deviation, making it more difficult to detect ^{10}Be from SPE within the ice core data. The difference between GCRminSMALL and GCRminBEST leads to a qualitative change between NGRIP and NEEM. Whereas for the GCRminBEST/GCRmaxBEST setting (which gives a GCR background signal at the drilling sites that is according to the ice core data and thus has been chosen as the setting for comparison with the data in Figures 10 and 11) the detectability at NEEM (violet line) is in general better than the detectability at NGRIP (green line), except for the peaks of SPE8/9/10. However, for the GCRminSMALL/GCRmaxSMALL setting this is opposite, with a better detectability of the SPE at NGRIP than at NEEM, where both aerosol settings show similar results for the detectability. The reason for this is that with the GCRminSMALL/GCRmaxSMALL setting, the surface flux at the poles and thus also above the drilling sites in Greenland for areas with low wet deposition is very small (see Figure 3), due to the lack of sedimentation because of the absence of larger aerosols in this tracer setting. As a result, the absolute values of the standard deviation of the deposition of ^{10}Be from GCR become small at NGRIP and thus the detectability with the GCRminSMALL/GCRmaxSMALL tracer setting becomes large.

This difference between GCRminSMALL/GCRmaxSMALL and GCRminBEST/GCRmaxBEST is even more pronounced for Dome Fuji (compare brown and orange line) for similar reasons. The detectability at Dome Fuji is 5–7 times higher in the GCRminSMALL/GCRmaxSMALL setting than for the more realistic GCRminBEST/GCRmaxBEST setting, meaning that even a five times smaller SPE (similar to the CE 774/775 SPE) could be detectable at Dome Fuji, if the GCRminSMALL/GCRmaxSMALL setting would be realistic (and sedimentation no major deposition factor in that region). At WDC the detectability in both settings is comparable and shows no large seasonal differences, like it was the case for NEEM.

Based on the above analysis of the detectability of SPEs in ^{10}Be ice core data, we are now able to define minimum scaling factors of an SPE like the one considered in this paper (CE 774/775 SPE based on GLE#69), assuming the detection threshold would be two times the standard deviation of the GCR background. According to the results in Table 5, the CE 774/775 SPE should not be detectable at Dome Fuji as a single drilling site, which seems plausible since the data shown in Figure 11 suggest a peak that can only be identified as such, when compared to peaks at other drilling sites within the respective time frame.

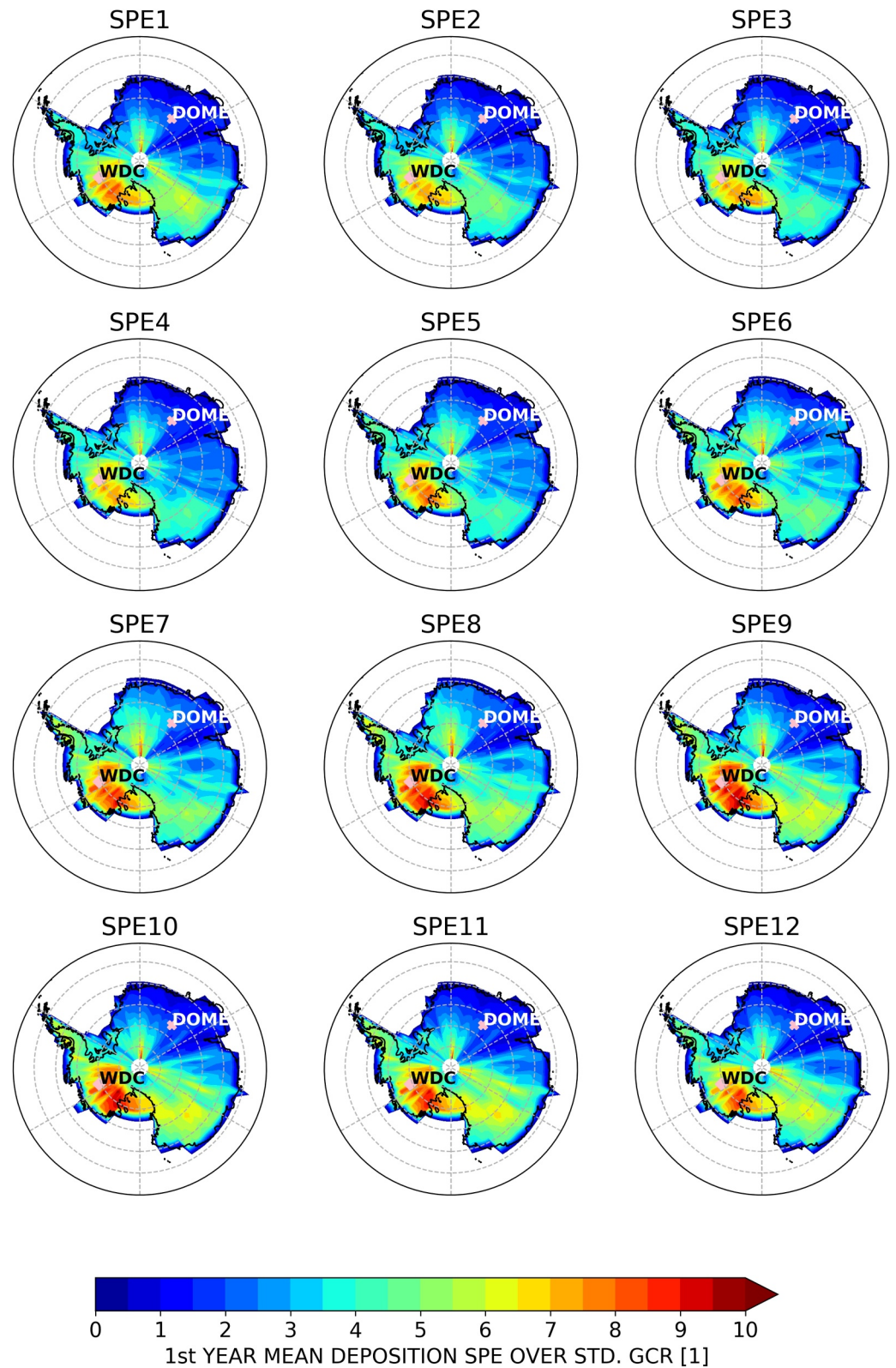


Figure 13. Same Figure as Figure 12, but for Dome Fuji and WDC (Antarctica).

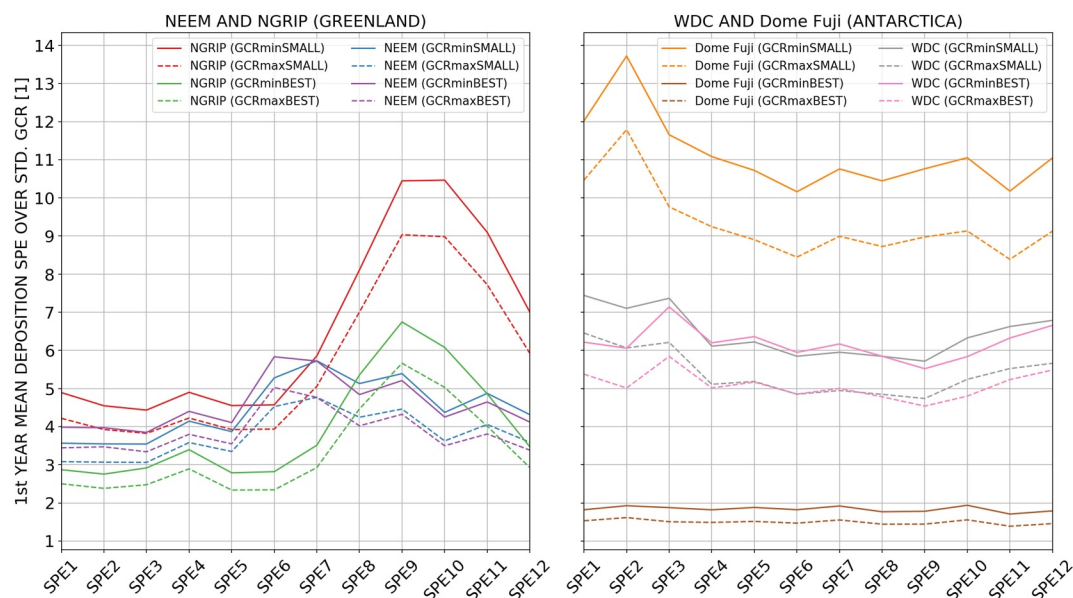


Figure 14. Detectability at NGRIP, NEEM, Dome Fuji and WDC for different tracer settings GCRminSMALL/BEST (solid lines) and GCRmaxSMALL/BEST (dashed lines).

Table 5 also suggests, that an SPE like the GLE#69 should be at least around half of the intensity of the CE 774/775 SPE, thus an event with a scaling factor of around 300 (from GLE#69) might be a bit too small to be detectable. Another SPE, the CE 992/993, that also has been detected in ice core data from the considered drilling sites (e.g., Mekhaldi et al., 2015), has a scaling factor around 2–3 times smaller than the CE 774/775 SPE, which means that, within our framework and simulations, it is at the lower border of detectability and more likely to be detected in the GCRmin phase occurring from summer to autumn.

5. Discussion and Summary

Using the state-of-the-art chemistry-climate model EMAC combined with input data for ^{10}Be from GCR and SEP calculated with PHITS, we modeled the production, atmospheric transport and surface deposition of ^{10}Be from two different sources, thus extending the approach of Spiegl et al. (2022). Our 3-dimensional model covers the full stratosphere and mesosphere (upper model border is 0.01 hPa), gives a realistic representation of all major stratospheric and tropospheric dynamics for mass transport, for example, BDC, STE, planetary wave activity, storm tracks, synoptic dynamics, and incorporates all deposition mechanisms important for the deposition of ^{10}Be , wet and dry deposition and sedimentation. Additionally, our model allowed us to test different scenarios for the production, transport and deposition of ^{10}Be . For ^{10}Be from SEP, we varied the month of initialization of the SPE to test the impact of seasonality on the detectability and for ^{10}Be from GCR, we changed the phase of the 11-year solar cycle such that the SPE can hit a maximum of the production rate or a minimum to investigate the difference between these two scenarios. Furthermore, we tested different combinations of stratospheric and

Table 5

Minimum Scaling Factors for Detecting an SPE Relative to CE 774/775 SPE From ^{10}Be in Ice Cores at Different Drilling Sites Occurring at the Minimum (GCRminBEST) or Maximum Phase (GCRmaxBEST) of GCR Production in the 11-Year Solar Cycle (e.g., for NEEM an SPE Occurring at the Minimum of GCR Production Needs to Be at Least 0.42 Times the CE 774/775 SPE to Be Detectable)

	NGRIP	NEEM	Dome Fuji	WDC
GCRminBEST	0.52 (0.38–0.67)	0.42 (0.32–0.52)	1.08 (1.03–1.17)	0.35 (0.33–0.38)
GCRmaxBEST	0.62 (0.47–0.78)	0.48 (0.38–0.60)	1.33 (1.23–1.43)	0.42 (0.40–0.45)

Note. The assumed threshold for detection is two standard deviations of GCR background deposition. Values are rounded. The range given in brackets represents the values for the least and the most detectable introduction month of the SPE.

tropospheric size distributions of the aerosols to which ^{10}Be couples after production, to study the impact of aerosol size on the transport and deposition of ^{10}Be . To evaluate our model setup, we compared our results for the surface flux of ^{10}Be with ice core reconstructions from Greenland and Antarctica and found an aerosol tracer setting (GCRmin/maxBEST) that sufficiently matches for both, the peak of the SPE and the GCR background surface flux in the ice core data.

Our results show differences in the deposition pattern of ^{10}Be for different aerosol size distributions, especially, regarding the role of sedimentation. For the setup with the same size distribution of aerosols in the troposphere like in the stratosphere (GCRmin/maxSMALL), sedimentation plays only a minor role compared to dry and especially wet deposition for all latitudes. However, if we go to larger aerosols in the troposphere, like it is the case for the BEST-setup, which is the setting that fits the proxy data from ice cores best, sedimentation plays a major role as a deposition mechanism, at least in the polar regions. For the high latitudes of the SH (Antarctica), sedimentation is the dominant deposition mechanism for the entire seasonal cycle. For the high latitudes of the NH (e.g., Greenland), sedimentation can exceed wet deposition as the most dominant deposition mechanism in NH winter (December to February), due to a combination of enhanced tracer downward transport from the BDC and lower precipitation, meaning less washout of tracers by wet deposition. Above 95% of the ^{10}Be deposited by sedimentation is produced in the troposphere (for the BEST setup).

The major role of sedimentation for the deposition of ^{10}Be in dependence on the aerosol size distribution in the troposphere (and stratosphere), is a new result of this study. This result is not only based on our simulations and the choice of reasonable aerosol size distributions for the stratosphere and troposphere, but also confirmed by the comparison to the empirical ice core data, because only the BEST setting reproduces the surface flux from GCR in the ice core data, meaning that sedimentation is required to explain the signal seen in the empirical data. The role of sedimentation in other model studies, for example, Field et al. (2006) or Heikkilä et al. (2013), has often been considered negligible compared to wet and dry deposition. With this study, we show that this is not necessarily true, depending on the size of the aerosols in the atmosphere as well as the latitude considered. Furthermore, our results suggest that drastic temporal changes in the size distribution of aerosols toward larger aerosols, for example, after large volcanic eruptions (Malinina et al., 2018), might be detectable in ^{10}Be ice core data. However, assuming lognormal distributions of aerosol size throughout the entire atmosphere is a simplification, which we chose as a technically clear, feasible and flexible approach fitting the needs of our simulations as a solid starting point. Therefore, simulations with for example, more realistic and complex aerosol models such as MADE3 (Kaiser et al., 2014) or GMXE (Pringle et al., 2010), could be a next step to compare the results to our results shown in this paper and further study the role of sedimentation for the deposition of ^{10}Be .

The global patterns of dry and wet deposition for ^{10}Be from GCR in our simulations are similar to those of former model studies (Field et al., 2006; Heikkilä et al., 2013). Wet deposition occurs basically at low latitudes and mid-latitudes driven by convective precipitation in the ITCZ and thus impact scavenging. Additionally, large areas of wet deposition occur south of Greenland and between Canada and Siberia, mainly resulting from large-scale precipitation and nucleation scavenging. Dry deposition is also present south of Greenland and between Canada and Siberia and around Antarctica. The main factor driving dry deposition in our simulations is the wind speed near the surface, which is particularly high above the open ocean (so in the areas mentioned before). The Pearson correlation between the near surface wind speed and dry deposition is as good as the correlation between precipitation and wet deposition (global value of around 0.6).

Our investigation of the deposition of ^{10}Be from GCR is the foundation of our results on the detectability of ^{10}Be from SEP in ice core data, which was defined as the ratio of the ^{10}Be signal of the SPE over the standard deviation of ^{10}Be from GCR at the considered location. The detectability of an SPE is fundamental for all studies on SPEs, but so far mostly the relation between the intensity and spectral hardness of an SPE with its detectability has been discussed (e.g., Mekhaldi et al., 2021). Here, we went further and investigated different factors impacting the detectability of SPEs similar to the CE 774/775 SPE (with given intensity and hardness).

The influence of the month of appearance of the SPE on the ^{10}Be surface flux at Greenland and Antarctica has been studied in detail in our former study (Spiegl et al., 2022). However, open questions remained regarding the impact of the seasonality on the detectability of the SPE, because the seasonality not only impacts the signal of the SPE but also the standard deviation of the ^{10}Be from GCR. Our results show that the detectability of an SPE can change considerably with the initialization month of the SPE, for example, the difference between the minimum and maximum detectability at NGRIP is a factor larger than 2. This implies that an SPE appearing in the month of

minimum detectability (SPE2/3) might not be detected in ^{10}Be ice core data at NGRIP, while an SPE appearing in the month of maximum detectability (SPE9/10) will be detected. The seasonal variations of the detectability are less pronounced for the other drilling sites considered, but still decisive for the question whether an SPE is detectable or not. Considering the whole area of Greenland and Antarctica, we also find large differences for the detectability depending on the location. It might, therefore, be possible to suggest positions of potential drillings sites, for example, a drilling site directly inside the low detectability area east of NGRIP might be a less useful choice for the detection of an SPE, whereas a drilling site close to NEEM or even south of NEEM, within the area of maximum detectability for SPE7 and SPE8, would allow also the detection of an SPE in ice cores that could not be detected in other areas of Greenland. However, multiple measurements from several different drilling sites are important to investigate the characteristics of an event.

The impact of the size of aerosols in the troposphere and stratosphere on the detectability was also tested for the two different scenarios GCRmin/maxSMALL and GCRmin/maxBEST, and the results show large differences for Dome Fuji and NGRIP. For both drilling sites the detectability is much higher for the GCRmin/maxSMALL setting, because without larger aerosols in the troposphere, the ^{10}Be surface flux from GCR becomes very low and thus also the values of the standard deviation. This effect is most pronounced for Dome Fuji, where the GCRmin/maxSMALL setting suggests a very high detectability of the SPE at Dome Fuji. However, this is not very realistic and not seen in the proxy data; in fact, the detectability of the CE 774/775 SPE at Dome Fuji is relatively low and below the detectability threshold of two times the standard deviation (which is, however, captured by the GCRmin/maxBEST setting). The detectability at WDC and NEEM is relatively similar for the two settings considered, meaning that sedimentation is less important for the deposition at these drilling sites.

To test the impact of the phase of the 11-year solar cycle which the SPE meets, we compared the scenarios GCRmin and GCRmax. Here we find that an SPE coinciding with the maximum phase of GCR production (GCRmax) is in general harder to detect than an SPE occurring during the minimum phase of ^{10}Be production (GCRmin). This could be of interest, as it is still an open question, whether SPEs (of a certain hardness) are more likely to occur in a certain phase of the 11-year solar cycle (e.g., Miyake et al., 2021; Zhang et al., 2022). The results of our study suggest that the detection of an SPE in ^{10}Be ice core data might be more difficult, if the SPE occurred during low solar activity (which is analogous to GCRmax). This could lead to the (maybe wrong) impression, that SPEs occur less often during low solar activity, while only their detectability is lower during that phase, which makes them more difficult/unlikely to detect. The lower detectability during low solar activity could give a biased impression of the correlation between SPEs and the phase of the 11-year solar cycle. However, note that Paleari et al. (2022) estimated that the CE 774/775 SPE occurred close to a solar minimum. Furthermore, note that in this study we investigated the detectability of an SPE occurring during low solar activity (GCRmax) and high solar activity (GCRmin), but also other phase of the 11-year solar cycle could be investigated, for example, when an SPE appears during the strongest decrease of solar activity (where the increase of the GCR production is the highest). This could be part of further investigations, to check if the increase of ^{10}Be production within the year in which the SPE occurs was any effect on the results.

Similar to the results of Spiegl et al. (2022), it has to be taken into account that our simulations assumed the preindustrial climate state of the year 1850 and a PI-climatology for SSTs. While the first assumption has consequences for the local meteorological parameters and dry and wet deposition, the latter dampens the inter-annual variability in the troposphere with consequences for the spread in the modeled annual mean ^{10}Be surface flux. Other assumptions and simplifications, besides the already discussed simplification for the aerosol description are for example, that the SPE considered (CE 774/775 SPE) is not representative for SPEs of other energetic spectra and thus the distribution of the ^{10}Be production between the stratosphere and troposphere. Additional effects of SPEs on the atmosphere, for example, the destruction of ozone and thus an impact on the radiation budget of the Earth, are also neglected. Furthermore, the GCR production of ^{10}Be was chosen to represent a phase of the solar activity that is assumed to have been present during the time of the CE 774/775 SPE. This, however, is not a complete representation of the full variability of GCR production or multiple decades of the 11-year solar cycle.

The model setup presented incorporates state-of-the-art climate modeling combined with complex input data for the production of ^{10}Be from GCR and SEP. This approach can be easily extended and applied for other SPE and GCR input data (also of other radionuclides), as well as other aerosol size distributions and even more sophisticated aerosol models. The results of simulations with for example, more sophisticated aerosol models could be

very interesting, because, although we do not expect fundamental changes in the global distribution of ^{10}Be as only large aerosols affect the vertical transport, some differences in local deposition pattern are likely. However, note that complex microphysical aerosol process might not be meaningful on a coarse grid point mesh as used by EMAC and furthermore that such microphysics are not very well understood to present date. In the next step, we will add a carbon cycle model to include ^{14}C , investigate the detectability of SPEs in tree rings and compare our model results to tree ring data. Furthermore, we will use the methods developed with this paper in transient simulations on ^7Be for the time span from 1850 to 2100.

Data Availability Statement

Data from the EMAC climate model simulations performed for this study are available at <http://dx.doi.org/10.17169/refubium-41306>. Data sources of the proxy-based reconstructions for the ^{10}Be surface flux at the different drilling locations are given in Miyake et al. (2015), Sigl et al. (2015), and Mekhaldi et al. (2015).

Acknowledgments

The authors would like to acknowledge the Institute for Space–Earth Environmental Research (ISEE) at the Nagoya University in Japan and the ISEE Joint Research Program for fruitful discussions and scientific exchange as well as the HLRN supercomputing facility in Berlin for the granted computing time and storage of data. Furthermore, we like to thank Holger Tost for giving advice regarding the wet deposition parametrization. Open Access funding enabled and organized by Projekt DEAL.

References

- Andrews, D. G., Holton, J. R., & Leovy, C. B. (1987). *Middle atmosphere dynamics* (p. 489). Academic Press.
- Appenzeller, C., Holton, J. R., & Rosenlof, K. H. (1996). Seasonal variation of mass transport across the tropopause. *Journal of Geophysical Research*, *101*(D10), 15071–15078. <https://doi.org/10.1029/96JD00821>
- Beer, J., Baumgartner, S., Dittrich-Hannen, B., Hauenstein, J., Kubik, P., Lukaszczuk, C., et al. (1994). Solar variability traced by cosmogenic isotopes. *International Astronomical Union Circular*, *143*, 291–300. <https://doi.org/10.1017/S0252921100024799>
- Beer, J., McCracken, K., & Steiger, R. (2012). *Cosmogenic radionuclides: Theory and applications in the terrestrial and space environments*. Springer Science & Business Media. <https://doi.org/10.1007/978-3-642-14651-0>
- Brehm, N., Bayliss, A., Christl, M., Synal, H. A., Adolphi, F., Beer, J., et al. (2021). Eleven-year solar cycles over the last millennium revealed by radiocarbon in tree rings. *Nature Geoscience*, *14*(1), 10–15. <https://doi.org/10.1038/s41561-020-00674-0>
- Brehm, N., Christl, M., Knowles, T. D. J., Casanova, E., Evershed, R. P., Adolphi, F., et al. (2022). Tree-rings reveal two strong solar proton events in 7176 and 5259 BCE. *Nature Communications*, *13*(1), 1196. <https://doi.org/10.1038/s41467-022-28804-9>
- Büntgen, U., Wacker, L., Galván, J. D., Arnold, S., Arseneault, D., Baillie, M., et al. (2018). Tree rings reveal globally coherent signature of cosmogenic radiocarbon events in 774 and 993 CE. *Nature Communications*, *9*(1), 1–7. <https://doi.org/10.1038/s41467-018-06036-0>
- Butchart, N. (2014). The Brewer-Dobson circulation. *Reviews of Geophysics*, *52*(2), 157–184. <https://doi.org/10.1002/2013RG000448>
- Delaygue, G., Bekki, S., & Bard, E. (2015). Modelling the stratospheric budget of beryllium isotopes. *Tellus B: Chemical and Physical Meteorology*, *67*(1), 28582. <https://doi.org/10.3402/tellusb.v67.28582>
- Deshler, T. (2008). A review of global stratospheric aerosol: Measurements, importance, life cycle, and local stratospheric aerosol. *Atmospheric Research*, *90*(2–4), 223–232. <https://doi.org/10.1016/j.atmosres.2008.03.016>
- Feely, H. W., Seitz, H., Lagomarsino, J., & Biscaye, P. E. (1966). Transport and fallout of stratospheric radioactive debris. *Tellus*, *18*(2–3), 316–328. <https://doi.org/10.3402/tellusa.v18i2-3.9619>
- Field, C., Schmidt, G., Koch, D., & Salyk, C. (2006). Modeling production and climate-related impacts on ^{10}Be concentration in ice cores. *Journal of Geophysical Research*, *111*(D15), D15107. <https://doi.org/10.1029/2005jd006410>
- Ganzeveld, L., & Lelieveld, J. (1995). Dry deposition parameterization in a chemistry general circulation model and its influence on the distribution of reactive trace gases. *Journal of Geophysical Research*, *100*(D10), 20999–21012. <https://doi.org/10.1029/95JD02266>
- Ganzeveld, L., Lelieveld, J., & Roelofs, G. J. (1998). A dry deposition parameterization for sulfur oxides in a chemistry and general circulation model. *Journal of Geophysical Research*, *103*(D5), 5679–5694. <https://doi.org/10.1029/97JD03077>
- Gleeson, L. J., & Axford, W. I. (1968). Solar modulation of galactic cosmic rays. *Astrophysical Journal*, *154*, 1011. <https://doi.org/10.1086/149822>
- Golubenko, K., Rozanov, E., Kovaltsov, G., & Usoskin, I. (2022). Zonal mean distribution of cosmogenic isotope (^7Be , ^{10}Be , ^{14}C , and ^{36}Cl) production in stratosphere and troposphere. *Journal of Geophysical Research: Atmospheres*, *127*(16), e2022JD036726. <https://doi.org/10.1029/2022JD036726>
- Heikkilä, U., Beer, J., Abreu, J. A., & Steinhilber, F. (2013). On the atmospheric transport and deposition of the cosmogenic radionuclides (^{10}Be): A review. *Space Science Reviews*, *176*(1–4), 321–332. <https://doi.org/10.1007/s11214-011-9838-0>
- Heikkilä, U., Beer, J., Jouzel, J., Feichter, J., & Kubik, P. (2008). ^{10}Be measured in a GRIP snow pit and modeled using the ECHAM5-HAM general circulation model. *Geophysical Research Letters*, *35*(5), L05817. <https://doi.org/10.1029/2007GL033067>
- Holton, J. R., Haynes, P. H., McIntyre, M. E., Douglass, A. R., Rood, R. B., & Pfister, L. (1995). Stratosphere-troposphere exchange. *Reviews of Geophysics*, *33*(4), 403–439. <https://doi.org/10.1029/95RG02097>
- Jöckel, P., Kerkweg, A., Buchholz-Dietsch, J., Tost, H., Sander, R., & Pozzer, A. (2008). Coupling of chemical processes with the Modular Earth Submodel System (MESSy) submodel TRACER. *Atmospheric Chemistry and Physics*, *8*(6), 1677–1687. <https://doi.org/10.5194/acp-8-1677-2008>
- Jöckel, P., Kerkweg, A., Pozzer, A., Sander, R., Tost, H., Riede, H., et al. (2010). Development cycle 2 of the modular Earth submodel system (MESSy2). *Geoscientific Model Development*, *3*, 717–752. <https://doi.org/10.5194/gmd-3-717-2010>
- Jöckel, P., Tost, H., Pozzer, A., Kunze, M., Kirner, O., Brenninkmeijer, C. A., et al. (2016). Earth system chemistry integrated modelling (ESCI-Mo) with the modular Earth submodel system (MESSy) version 2.51. *Geoscientific Model Development*, *9*(3), 1153–1200. <https://doi.org/10.5194/gmd-9-1153-2016>
- Junge, C. E. (1963). Air chemistry and radioactivity. In *International Geophysics Series* (Vol. 4). Academic Press. [https://doi.org/10.1016/s0074-6142\(08\)x6045-0](https://doi.org/10.1016/s0074-6142(08)x6045-0)
- Kaiser, J. C., Hendricks, J., Righi, M., Riemer, N., Zaveri, R. A., Metzger, S., & Aquila, V. (2014). The MESSy aerosol submodel MADE3 (v2.0b): Description and a box model test. *Geoscientific Model Development*, *7*(3), 1137–1157. <https://doi.org/10.5194/gmd-7-1137-2014>
- Kerkweg, A., Buchholz, J., Ganzeveld, L., Pozzer, A., Tost, H., & Jöckel, P. (2006). An implementation of the dry removal processes DRY DEPOSITION and SEDIMENTATION in the Modular Earth Submodel System (MESSy). *Atmospheric Chemistry and Physics*, *6*(12), 4617–4632. <https://doi.org/10.5194/acp-6-4617-2006>

- Koldobskiy, S., Mekhaldi, F., Kovaltsov, G., & Usoskin, I. (2023). Multiproxy reconstructions of integral energy spectra for extreme solar particle events of 7176 BCE, 660 BCE, 775 CE, and 994 CE. *Journal of Geophysical Research: Space Physics*, 128(3), e2022JA031186. <https://doi.org/10.1029/2022JA031186>
- Kovaltsov, G. A., & Usoskin, I. G. (2010). A new 3D numerical model of cosmogenic nuclide ^{10}Be production in the atmosphere. *Earth and Planetary Science Letters*, 291(1–4), 182–188. <https://doi.org/10.1016/j.epsl.2010.01.011>
- Lifton, N., Sato, T., & Dunai, T. (2014). Scaling *in situ* cosmogenic nuclide production rates using analytical approximations to atmospheric cosmic-ray fluxes. *Earth and Planetary Science Letters*, 386, 149–160. <https://doi.org/10.1016/j.epsl.2013.10.052>
- Malinina, E., Rozanov, A., Rozanov, V., Liebing, P., Bovensmann, H., & Burrows, J. P. (2018). Aerosol particle size distribution in the stratosphere retrieved from SCIAMACHY limb measurements. *Atmospheric Measurement Techniques*, 11(4), 2085–2100. <https://doi.org/10.5194/amt-11-2085-2018>
- Masarik, J., & Beer, J. (1999). Simulation of particle fluxes and cosmogenic nuclide production in the Earth's atmosphere. *Journal of Geophysical Research*, 104(D10), 12099–12111. <https://doi.org/10.1029/1998JD200091>
- Matthes, K., Funke, B., Andersson, M. E., Barnard, L., Beer, J., Charbonneau, P., et al. (2017). Solar forcing for CMIP6 (v3. 2). *Geoscientific Model Development*, 10(6), 2247–2302. <https://doi.org/10.5194/gmd-10-2247-2017>
- Mekhaldi, F., Adolphi, F., Herbst, K., & Muscheler, R. (2021). The signal of solar storms embedded in cosmogenic radionuclides: Detectability and uncertainties. *Journal of Geophysical Research: Space Physics*, 126(8), e2021JA029351. <https://doi.org/10.1029/2021JA029351>
- Mekhaldi, F., Muscheler, R., Adolphi, F., Aldahan, A., Beer, J., McConnell, J. R., et al. (2015). Multiradionuclide evidence for the solar origin of the cosmic-ray events of AD 774/5 and 993/4. *Nature Communications*, 6(1), 1–8. <https://doi.org/10.1038/ncomms9611>
- Melott, A. L., & Thomas, B. C. (2012). Causes of an AD 774–775 ^{14}C increase. *Nature*, 491(7426), E1–E2. <https://doi.org/10.1038/nature11695>
- Miyahara, H., Tokanai, F., Moriya, T., Takeyama, M., Sakurai, H., Ohya, M., et al. (2022). Recurrent large-scale solar proton events before the onset of the Wolf grand solar minimum. *Geophysical Research Letters*, 49(5), e2021GL097201. <https://doi.org/10.1029/2021GL097201>
- Miyake, F., Masuda, K., & Nakamura, T. (2013). Another rapid event in the carbon-14 content of tree rings. *Nature Communications*, 4(1), 1748. <https://doi.org/10.1038/ncomms2783>
- Miyake, F., Nagaya, K., Masuda, K., & Nakamura, T. (2012). A signature of cosmic-ray increase in AD 774–775 from tree rings in Japan. *Nature*, 486(7402), 240–242. <https://doi.org/10.1038/nature1123>
- Miyake, F., Panyushkina, I. P., Jull, A. J. T., Adolphi, F., Brehm, N., Helama, S., et al. (2021). A single-year cosmic ray event at 5410 BCE registered in ^{14}C of tree rings. *Geophysical Research Letters*, 48(11), e2021GL093419. <https://doi.org/10.1029/2021GL093419>
- Miyake, F., Suzuki, A., Masuda, K., Horiuchi, K., Motoyama, H., Matsuzaki, H., et al. (2015). Cosmic ray event of AD 774–775 shown in quasi-annual ^{10}Be data from the Antarctic Dome Fuji ice core. *Geophysical Research Letters*, 42(1), 84–89. <https://doi.org/10.1002/2014GL062218>
- Oberländer-Hayn, S., Meul, S., Langematz, U., Abalichin, J., & Haanel, F. (2015). A chemistry-climate model study of past changes in the Brewer-Dobson circulation. *Journal of Geophysical Research: Atmospheres*, 120(14), 6742–6757. <https://doi.org/10.1002/2014JD022843>
- O'Hare, P., Mekhaldi, F., Adolphi, F., Raisbeck, G., Aldahan, A., Anderberg, E., et al. (2019). Multiradionuclide evidence for an extreme solar proton event around 2,610 BP (~ 660 BC). *Proceedings of the National Academy of Sciences*, 116(13), 5961–5966. <https://doi.org/10.1073/pnas.1815725116>
- Ohata, S., Moteki, N., Mori, T., Koike, M., & Kondo, Y. (2016). A key process controlling the wet removal of aerosols: New observational evidence. *Sci. Rep.-UK*, 6(1), 34113. <https://doi.org/10.1038/srep34113>
- Paleari, C. I., Mekhaldi, F., Adolphi, F., Christl, M., Vockenhuber, C., Gautschi, P., et al. (2022). Cosmogenic radionuclides reveal an extreme solar particle storm near a solar minimum 9125 years BP. *Nature Communications*, 13(1), 214. <https://doi.org/10.1038/s41467-021-27891-4>
- Pandis, S. N., Wexler, A. S., & Seinfeld, J. H. (1995). Dynamics of tropospheric aerosols. *The Journal of Physical Chemistry*, 99(24), 9646–9659. <https://doi.org/10.1021/j100024a003>
- Park, J., Southon, J., Fahrni, S., Creasman, P., & Mewaldt, R. (2017). Relationship between solar activity and $\Delta^{14}\text{C}$ peaks in AD 775, AD 994, and 660 BC. *Radiocarbon*, 59(4), 1147–1156. <https://doi.org/10.1017/RDC.2017.59>
- Pozzer, A., Jöckel, P., Kern, B., & Haak, H. (2011). The atmosphere-ocean general circulation model EMAC-MPIOM. *Geoscientific Model Development*, 4(3), 771–784. <https://doi.org/10.5194/gmd-4-771-2011>
- Pringle, K. J., Tost, H., Steil, B., Giannadaki, D., Nenes, A., Fountoukis, C., et al. (2010). Description and evaluation of GMXe: A new aerosol submodel for global simulations (v1). *Geoscientific Model Development*, 3(2), 391–412. <https://doi.org/10.5194/gmd-3-391-2010>
- Roekner, E., Brokopf, R., Esch, M., Giorgetta, M., Hagemann, S., Kornbluh, L., et al. (2006). Sensitivity of simulated climate to horizontal and vertical resolution in the ECHAM5 atmosphere model. *Journal of Climate*, 19(16), 3771–3791. <https://doi.org/10.1175/JCL13824.1>
- Sakurai, H., Tokanai, F., Miyake, F., Horiuchi, K., Masuda, K., Miyahara, H., et al. (2020). Prolonged production of ^{14}C during the ~ 660 BCE solar proton event from Japanese tree rings. *Scientific Reports*, 10(1), 660. <https://doi.org/10.1038/s41598-019-57273-2>
- Sato, T. (2015). Analytical model for estimating terrestrial cosmic ray fluxes nearly anytime and anywhere in the world: Extension of PARMA/EXPACS. *PLoS One*, 10(12), e0144679. <https://doi.org/10.1371/journal.pone.0144679>
- Sato, T. (2016). Analytical model for estimating the zenith angle dependence of terrestrial cosmic ray fluxes. *PLoS One*, 11(8), e0160390. <https://doi.org/10.1371/journal.pone.0160390>
- Sato, T., Iwamoto, Y., Hashimoto, S., Ogawa, T., Furuta, T., Abe, S. I., et al. (2018). Features of particle and heavy ion transport code system (PHITS) version 3.02. *Journal of Nuclear Science and Technology*, 55(6), 684–690. <https://doi.org/10.1080/00223131.2017.1419890>
- Sato, T., Kataoka, R., Shiota, D., Kubo, Y., Ishii, M., Yasuda, H., et al. (2018). Real-time and automatic analysis Program for WASAVIES: Warning system for aviation exposure to solar energetic particles. *Space Weather*, 16(7), 924–936. <https://doi.org/10.1029/2018SW001873>
- Sato, T., Yasuda, H., Niita, K., Endo, A., & Sihver, L. (2008). Development of PARMA: PHITS-based analytical radiation model in the atmosphere. *Radiation Research*, 170(2), 244–259. <https://doi.org/10.1667/RR1094.1>
- Sigl, M., Winstrup, M., McConell, J. R., Welten, K. C., Plunkett, G., Ludlow, F., et al. (2015). Timing and climate forcing of volcanic eruptions for the past 2,500 years. *Nature*, 523(7562), 543–549. <https://doi.org/10.1038/nature14565>
- Spiegel, T. C., Yoden, S., Langematz, U., Sato, T., Chhin, R., Noda, S., et al. (2022). Modeling the transport and deposition of ^{10}Be produced by the strongest solar proton event during the Holocene. *Journal of Geophysical Research: Atmospheres*, 127(13), e2021JD035658. <https://doi.org/10.1029/2021JD035658>
- Stohl, A., Bonasoni, P., Cristofanelli, P., Collins, W., Feichter, J., Frank, A., et al. (2003). Stratosphere-troposphere exchange: A review, and what we have learned from STACCATO. *Journal of Geophysical Research*, 108(D12), 8516. <https://doi.org/10.1029/2002JD002490>
- Sukhodolov, T., Usoskin, I., Rozanov, E., Asvestari, E., Ball, W. T., Curran, M. A., et al. (2017). Atmospheric impacts of the strongest known solar particle storm of 775 AD. *Scientific Reports*, 7(1), 1–9. <https://doi.org/10.1038/srep45257>
- Terrasi, F., Marzaioli, F., Buompane, R., Passariello, I., Porzio, G., Capano, M., et al. (2020). Can the ^{14}C production in 1055 CE be affected by SN1054? *Radiocarbon*, 62(5), 1403–1418. <https://doi.org/10.1017/RDC.2020.58>

- Terzi, L., & Kalinowski, M. (2017). World-wide seasonal variation of ^7Be related to large-scale atmospheric circulation dynamics. *Journal of Environmental Radioactivity*, 178(179), 1–15. <https://doi.org/10.1016/j.jenvrad.2017.06.031>
- Tost, H., Jöckel, P., Kerkweg, A., Sander, R., & Lelieveld, J. (2006). Technical note: A new comprehensive SCAVenging submodel for global atmospheric chemistry modelling. *Atmospheric Chemistry and Physics*, 6(3), 565–574. <https://doi.org/10.5194/acp-6-565-2006>
- Usoskin, I., Miyake, F., Baroni, M., Brehm, N., Dalla, S., Hayakawa, H., et al. (2023). Extreme solar events: Setting up a paradigm. *Space Science Reviews*, 219(8), 73. <https://doi.org/10.1007/s11214-023-01018-1>
- Usoskin, I. G. (2017). A history of solar activity over millennia. *Living Reviews in Solar Physics*, 14(1), 3. <https://doi.org/10.1007/s41116-017-0006-9>
- Usoskin, I. G., Koldobskiy, S. A., Kovaltsov, G. A., Rozanov, E. V., Sukhodolov, T. V., Mishev, A. L., & Mironova, I. A. (2020). Revisited reference solar proton event of 23 February 1956: Assessment of the cosmogenic-isotope method sensitivity to extreme solar events. *Journal of Geophysical Research: Space Physics*, 125(6), e2020JA027921. <https://doi.org/10.1029/2020JA027921>
- Usoskin, I. G., Kromer, B., Ludlow, F., Beer, J., Friedrich, M., Kovaltsov, G. A., et al. (2013). The AD775 cosmic event revisited: The Sun is to blame. *Astronomy & Astrophysics*, 552, L3. <https://doi.org/10.1051/0004-6361/201321080>
- Usoskin, I. G., Solanki, S. K., Kovaltsov, G. A., Beer, J., & Kromer, B. (2006). Solar proton events in cosmogenic isotope data. *Geophysical Research Letters*, 33(8), L08107. <https://doi.org/10.1029/2006GL026059>
- Wernli, H., & Bourqui, M. (2002). A Lagrangian “1-year climatology” of (deep) cross-tropopause exchange in the extratropical Northern Hemisphere. *Journal of Geophysical Research*, 107(D2), ACL13-1–ACL13-16. <https://doi.org/10.1029/2001JD000812>
- Wesely, M. (1989). Parameterization of surface resistances to gaseous dry deposition in regional-scale numerical models. *Atmospheric Environment*, 23(6), 1293–1304. [https://doi.org/10.1016/0004-6981\(89\)90153-4](https://doi.org/10.1016/0004-6981(89)90153-4)
- Yamagata, T., Nagai, H., Matsuzaki, H., & Narasaki, Y. (2019). Decadal variations of atmospheric ^7Be and ^{10}Be concentrations between 1998 and 2014 in Japan. *Nuclear Instruments and Methods in Physics Research Section B: Beam Interactions with Materials and Atoms*, 455, 265–270. <https://doi.org/10.1016/j.nimb.2018.12.029>
- Zhang, Q., Sharma, U., Dennis, J. A., Scifo, A., Kuitens, M., Büntgen, U., et al. (2022). Modelling cosmic radiation events in the tree-ring radiocarbon record. *Proceedings of the Royal Society A*, 478(2266), 20220497. <https://doi.org/10.1098/rspa.2022.0497>
- Zheng, M., Adolphi, F., Sjolte, J., Aldahan, A., Possnert, G., Wu, M., et al. (2020). Solar and climate signals revealed by seasonal ^{10}Be data from the NEEEM ice core project for the neutron monitor period. *Earth and Planetary Science Letters*, 541, 116273. <https://doi.org/10.1016/j.epsl.2020.116273>